



Release of mitochondrial dsRNA into the cytosol is a key driver of the inflammatory phenotype of senescent cells

Received: 20 October 2023

Accepted: 6 August 2024

Published online: 27 August 2024

Check for updates

Vanessa López-Polo , Mate Maus , Emmanouil Zacharioudakis³, Miguel Lafarga⁴, Camille Stephan-Otto Attolini , Francisco D. M. Marques³, Marta Kovatcheva , Evripidis Gavathiotis & Manuel Serrano

The escape of mitochondrial double-stranded dsRNA (mt-dsRNA) into the cytosol has been recently linked to a number of inflammatory diseases. Here, we report that the release of mt-dsRNA into the cytosol is a general feature of senescent cells and a critical driver of their inflammatory secretome, known as senescence-associated secretory phenotype (SASP). Inhibition of the mitochondrial RNA polymerase, the dsRNA sensors RIGI and MDA5, or the master inflammatory signaling protein MAVS, all result in reduced expression of the SASP, while broadly preserving other hallmarks of senescence. Moreover, senescent cells are hypersensitized to mt-dsRNA-driven inflammation due to their reduced levels of PNPT1 and ADAR1, two proteins critical for mitigating the accumulation of mt-dsRNA and the inflammatory potency of dsRNA, respectively. We find that mitofusin MFN1, but not MFN2, is important for the activation of the mt-dsRNA/MAVS/SASP axis and, accordingly, genetic or pharmacologic MFN1 inhibition attenuates the SASP. Finally, we report that senescent cells within fibrotic and aged tissues present dsRNA foci, and inhibition of mitochondrial RNA polymerase reduces systemic inflammation associated to senescence. In conclusion, we uncover the mt-dsRNA/MAVS/MFN1 axis as a key driver of the SASP and we identify novel therapeutic strategies for senescence-associated diseases.

Cellular senescence is an evolutionary conserved and stereotypic response characterized by an inability to proliferate and by the secretion of pro-inflammatory factors, the latter collectively known as the senescence-associated secretory phenotype (SASP)¹. Cellular senescence is elicited by multiple stresses, including aberrant oncogene expression, DNA damage, reactive oxygen species, and telomeric erosion¹. In young, healthy, organisms, senescent cells are short-lived

due to their immune clearance, mainly by macrophages and natural killer (NK) cells². However, in aged organisms or in immunosuppressive environments, immune clearance fails and senescent cells accumulate, as it happens in a broad variety of diseases and in aged tissues¹⁻³. Senescent cells directly contribute to the aggravation and progression of multiple diseases and this is mainly due to their continued release of the SASP⁴. Importantly, there is growing evidence,

¹Institute for Research in Biomedicine (IRB Barcelona), Barcelona Institute of Science and Technology (BIST), Barcelona, Spain. ²Vall d'Hebron Institute of Oncology (VHIO), Barcelona, Spain. ³Department of Biochemistry, Department of Medicine, Department of Oncology, Montefiore Einstein Comprehensive Cancer Center, Institute for Aging Research, Wilf Family Cardiovascular Research Institute, Albert Einstein College of Medicine, Bronx, NY, USA. ⁴Department of Anatomy and Cell Biology and Centro de Investigación Biomédica en Red sobre Enfermedades Neurodegenerativas (CIBERNED), University of Cantabria-IDIVAL, Santander, Spain. ⁵IFOM ETS – The AIRC Institute of Molecular Oncology, Milan, Italy. ⁶Altos Labs, Cambridge Institute of Science, Granta Park, UK. e-mail: mserrano@altoslabs.com

both in animal models and also in patients, that senescence-targeting strategies are efficient against multiple diseases^{1,3,4}.

Emerging evidence has pointed to the mitochondria of senescent cells as one of the principal modulators of the SASP⁵. Specifically, cells with severe disruption of mitochondrial functions, such as inhibition of the electron transport chain, or ablation of mitochondrial protein chaperones, undergo an atypical senescence that lacks the full SASP secretome⁶. In an even more striking demonstration of this concept, cells devoided of mitochondria due to forced mitophagy fail to activate the SASP upon exposure to senescence-inducing triggers⁷. The nature of the SASP-inducing signals emanating from the mitochondria is only partially understood. The mitochondria of senescent cells produce high levels of ROS that activate innate immune signaling hubs⁸. More recently, it has been reported that senescent cells release mitochondrial double-stranded DNA (mt-dsDNA) into the cytosol through transient BAX/BAK pores, and this cytosolic mt-dsDNA contributes to the SASP via activation of the cGAS/STING pathway⁹. Moreover, during aging, senescent cells release mitochondrial DNA fragments detectable in the serum, which also contribute to systemic inflammation¹⁰. The above findings on senescent cells are part of a larger body of evidence linking the release of mt-dsDNA to the cytosol as a critical inflammatory event of relevance in multiple contexts and diseases^{11–13}.

Mitochondria have the peculiarity of generating double-stranded RNA (dsRNA) molecules as a result of the normal process of bidirectional and overlapping transcription of its circular genome. There are dedicated mechanisms to separate the two strands and ensure the stability of the H strand, which is almost entirely coding, and the degradation of the L strand, which is largely non-coding¹⁴. The majority of the L strand undergoes rapid decay by the RNA degradosome complex containing the ribonuclease PNPase (encoded by *PNPT1*)¹⁴. Importantly, perturbations in mitochondrial RNA processing may cause abnormal accumulation of mt-dsRNA, its release through BAX/BAK pores, and the activation of innate immune signaling pathways¹⁵. This is the case of cells from patients with Aicardi-Goutières or Leigh syndromes carrying loss-of-function mutations in the *PNPT1* gene and, as a consequence, presenting aberrant constitutive activation of interferon type I signaling¹⁵. The release of mt-dsRNA has also been reported in osteoarthritis¹⁶, renal injury¹⁷, and Huntington's disease¹⁸. Also, the inflammatory response elicited by genotoxic agents has been reported to be mostly due to the damage inflicted on the mt-dsDNA, which in turn results in the cytosolic release of mitochondrial RNA through BAX/BAK pores¹⁹. Another gene linked to the Aicardi-Goutières syndrome is *ADAR*, which encodes a dsRNA-binding protein with adenosine deaminase activity, and whose main function is to reduce the inflammatory activity of cytosolic dsRNA²⁰. The presence of mt-dsRNAs in the cytosol is a potent inflammatory trigger through the activation of sensors RIG-I and MDA5, and the oligomerization of MAVS on the mitochondrial surface, which serves as a platform to activate the interferon and NFκB signaling pathways²¹.

Here, we show that mt-dsRNA-driven inflammation is a general feature of cellular senescence and, therefore, relevant to multiple aging-associated diseases. We also identify a number of drug-actionable targets whose inhibition strongly reduces the pro-inflammatory secretome of senescent cells.

Results

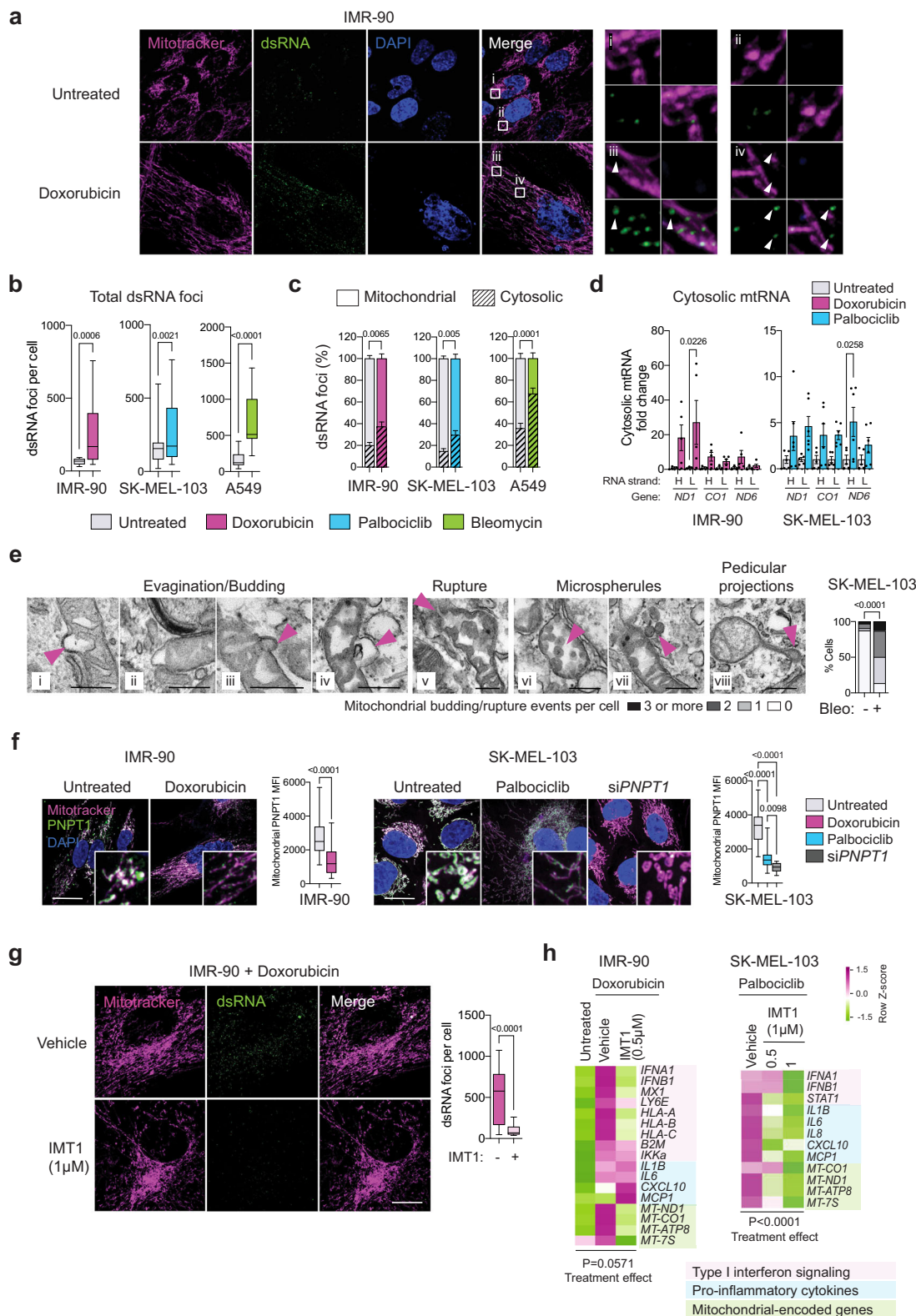
Senescent cells release mitochondrial dsRNA into the cytosol

Given the large body of evidence linking mt-dsRNA with inflammation^{23–29}, we hypothesized that mt-dsRNA could also be released into the cytosol from senescent mitochondria. To test this, we detected dsRNA by immunofluorescence using monoclonal antibody (J2)²². To confirm the specificity of J2 against dsRNA, we treated proliferating cells with the general transcriptional inhibitor actinomycin D

(ActD) and this completely eliminated J2 foci, while siRNA-mediated inhibition of *PNPT1* (encoding a key enzyme that prevents the accumulation of mt-dsRNA¹⁵) resulted in a robust increase in J2 foci (Supplementary Fig. 1a). Then, we induced senescence in three different human cell types, IMR-90 lung fibroblasts using the DNA damaging agent doxorubicin, SK-MEL-103 melanoma cells treating them with the CDK4/6 inhibitor palbociclib, and A549 lung adenocarcinoma cells exposing them to the genotoxic agent bleomycin. These cellular models were chosen for their efficiency in inducing senescence, and also because they cover a variety of cell types and senescence triggers. Senescence was confirmed by senescence-associated β-galactosidase (SABG) staining and by measuring the expression of senescence-associated genes *CDKN1A* and *IL6* by RT-qPCR (Supplementary Fig. 1b, c). As previously described⁵, we observed that senescent cells have an increased mitochondrial mass, increased mitochondrial DNA copy number, and decreased mitochondrial membrane potential (Supplementary Fig. 1d–f). Interestingly, staining with J2 revealed a significant accumulation of dsRNA foci in senescent cells compared to their proliferative counterparts (Fig. 1a, b; Supplementary Fig. 1g–h). A tendency to accumulate mt-dsRNA is detectable as early as day 3 after the senescence-inducing treatment and a significant increase was observed at day 7, coincident with the full establishment of senescence (Supplementary Fig. 1i). By co-staining cells with a mitochondria-specific probe, we quantified the proportion of J2 foci localized within or outside of mitochondria. Interestingly senescent cells presented a significant increase in extra-mitochondrial dsRNA compared to proliferative cells (Fig. 1c). To assess the possible mitochondrial origin of these cytosolic dsRNA foci, we isolated RNA from mitochondria-free cytosolic fractions of proliferative and senescent cells. Of note, our cytosolic fractions lacked detectable mitochondrial protein AIF, suggesting the absence of mitochondrial contamination and also that the fractionation method did not cause major mitochondrial membrane rupture (Supplementary Fig. 1j). By strand-specific quantitative PCR, we observed that the cytosolic fractions from senescent cells contained higher levels of each of the two mitochondrial RNA strands, H and L, compared to proliferative cells (Fig. 1d). Given the importance of the above observations, we confirmed them in additional models of cellular senescence, in particular, irradiation-induced senescence and replicative senescence in human and mouse fibroblasts (Supplementary Fig. 2a–e).

The release of mt-dsDNA in acutely damaged cells occurs through large mitochondrial evaginations that rupture and extrude the mitochondrial matrix content into the cytosol^{23,24}. These evaginations could conceivably allow the release of mt-dsRNA and, for this reason, we wondered if we could detect mitochondrial evaginations in senescent cells. Electron microscopy analysis revealed that the mitochondria of senescent cells present budding structures, some including the matrix and even others showing evidence of rupture (Fig. 1e). In addition to identifying evagination and budding structures, we observed pedicular projections on the membrane of mitochondria in senescent cells, as well as the formation of "microspherules" within the matrix and their potential release into the cytosol (Fig. 1e). These abnormalities were observed in the majority of senescent cells (87% of the cells with at least one mitochondrial budding event) which was in contrast with the low frequency in the parental non-senescent cells (13% of cells with at least one event). Interestingly, we observed a significant reduction in the protein levels of PNPT1 detected by immunofluorescence in senescent cells compared to non-senescent cells (Fig. 1f). Reduced levels of PNPT1 could be one of the factors that contribute to the accumulation of mt-dsRNA in senescent cells.

Collectively, we conclude that the mitochondria of senescent cells accumulate abnormally high levels of dsRNA that are released to the cytosol.



Pharmacologic inhibition of mitochondrial RNA polymerase reduces the SASP

Considering the link between mt-dsRNA release and the constitutive inflammation that characterizes the Aicardi-Goutières and the Leigh syndromes^{20,25}, we wondered if the release of mt-dsRNA could also underlie the inflammatory phenotype of senescent cells. We took advantage of a highly specific inhibitor of mitochondrial RNA

polymerase, named IMT1²⁶. Senescent cells were further exposed to IMT1 for 48 h prior to analysis. As expected, inhibition of mitochondrial RNA polymerase activity resulted in a profound reduction in the levels of dsRNAs (detected by J2) (Fig. 1g) and, mitochondrial-encoded mRNAs (*MT-ND1*, *MT-CO1*, and *MT-ATP8*) (Fig. 1h). Importantly, treatment of senescent cells with IMT1 also reduced the mRNA levels of SASP factors in SK-MEL-103 cells and type-I

Fig. 1 | Senescent cells present increased mt-dsRNA that leaks into the cytosol.

a Immunostaining of dsRNA (green) in untreated IMR-90 cells or exposed to doxorubicin. Mitochondria (magenta) and nuclei (blue) are stained with Mito-Tracker and DAPI, respectively. Arrowhead indicates dsRNA foci outside mitochondria. **b** Quantification of dsRNA foci per cell in IMR-90, SK-MEL-103 and A549 cells, untreated or exposed to various senescence-inducing stimuli. **c** Graphs quantify the colocalization of dsRNA (J2 foci) with mitochondria (mitotracker). **d** RT-qPCR analysis of mtRNA heavy (H) and light (L) strands in cytosolic fractions of senescent IMR-90 exposed to doxorubicin or senescent SK-MEL-103 cells treated with palbociclib for 7 days. The names of the genes indicate the location of the RNA segment amplified. Data expressed as fold change respect untreated cells. **e** Transmission electron microscopy images of senescent SK-MEL-103 cells exposed to bleomycin. **i** Evagination with vesiculation of juxtaposed outer and inner membranes. **ii** Evagination with vesiculation only of the outer membrane and focal disruption of the inner membrane. **iii** Evagination of juxtaposed outer and inner membranes, with amorphous material of moderate electron density corresponding to the extrusion of the mitochondrial matrix. **iv** Large evagination of the outer membrane and budding of the inner membrane. **v** Focal disruption of the mitochondrial membranes with apparent release of matrix components into the cytosol. **vi** Disruption of mitochondrial structure with segregation of the matrix into free microspherules. **vii** Possible release of matrix microspherules, bounded by the inner membrane, into the cytosol. **viii** Long “Pedicular” projection of mitochondrial membranes with extrusion of the matrix at the tip. Arrowhead indicates mitochondrial budding structures, projections, microspherules, or ruptures. **f** Super-resolution AiryScan microscopy images of PNPT1 (green) in IMR-90 and SK-MEL-103 cells exposed to different senescent stimuli, untreated or transfected with siPNPT1 for 2 days. Mitochondria (magenta) were stained with MitoTracker. Graph quantify PNPT1 mean fluorescence intensity (MFI) in the mitochondrial surface. **g** Immunostaining of dsRNA (green) in IMR-90 cells exposed to doxorubicin for 7 days and treated with IMT1 (1 μM) or vehicle (DMSO) for 48 h. Mitochondria (magenta) is stained with MitoTracker. The graph shows the quantification of

dsRNA foci per cell. **h** Heatmaps showing the alteration in SASP factors. Senescence was induced for 3 days in IMR-90 cells by doxorubicin and in SK-MEL-103 by palbociclib and then treated with IMT1 or vehicle for 48 h. Non-senescent cells treated with vehicle were used as control. Data was generated measuring mRNA levels by qPCR and normalized to *B-ACTIN* from 3 to 5 independent replicates and Z score has been calculated for each gene (row). The colored scale bar shown at the upper right indicates relative expression values, where -1.5 (green) and 1.5 (magenta) represent under- and over-abundance, respectively. In the box plots in **(b)**, **(f)**, and **(g)**, the lower and upper boundaries of the box represent the first and third quartiles, with the median indicated by a line inside the box. The whiskers extend to the maximum and minimum values. Data show mean ± SEM in **(c)**, **(d)**; mean in **(h)**; Comparisons by two-sided *t*-test for **(b)**, **(f)** (IMR-90); two-way ANOVA followed by Šidák's multiple comparisons test for **(d)**; two-sided chi-square for **(e)**; one-way ANOVA followed by Tukey's multiple comparisons test for **(f)** (SK-MEL-103); two-way ANOVA for **(h)** revealed a significant main effect of the treatment factor ($F(2, 215) = 3.536, P = 0.0308$) in IMR-90 and ($F(1, 48) = 37.5, P < 0.0001$) in SK-MEL-103. Exact *p*-values are shown in all panels. Sample numbers were $n = 18$ (untreated, IMR-90), $n = 20$ (doxorubicin, IMR-90), $n = 50$ (untreated, SK-MEL-103), $n = 19$ (palbociclib, SK-MEL-103), $n = 17$ (untreated, A549), $n = 9$ (bleomycin, A549), cells analyzed from 3 independent replicates for **(b)**; $n = 14$ (untreated, IMR-90), $n = 19$ (doxorubicin, IMR-90), $n = 32$ (untreated, SK-MEL-103), $n = 11$ (palbociclib, SK-MEL-103), $n = 10$ (untreated, A549), $n = 13$ (bleomycin, A549), cells analyzed from 3 independent replicates for **(c)**; $n = 5$ independent replicates (IMR-90) and $n = 6$ independent replicates (SK-MEL-103) for **(d)**; $n = 31$ (untreated) and $n = 31$ (bleomycin) cells analyzed from 1 experiment for **(e)**; $n = 46$ (untreated, IMR-90), $n = 21$ (doxorubicin, IMR-90) $n = 41$ (untreated, SK-MEL-103), $n = 37$ (palbociclib, SK-MEL-103) cells analyzed from 3 independent replicates in **(f)**; $n = 36$ (vehicle), $n = 26$ (IMT1) cells analyzed from 3 independent replicates for **(g)**; $n = 7$ independent replicates for **(h)**. Representative images are shown. Scale bars are all 20 μm except 250 nm for **(e)**. Source data are provided as a Source Data file.

interferons in IMR-90 cells (Fig. 1h). At increasing concentrations of IMT1, mitochondrial RNA levels were progressively reduced together with a proportional reduction in *IFNA1* mRNA levels (Supplementary Fig. 3a, b). In contrast to mitochondrial RNA, the mRNA levels of nuclear-encoded mitochondrial genes were not affected by IMT1 (Fig. 1h; Supplementary Fig. 3a–c). Also, the levels of *CDKN1A* (encoding the cell-cycle inhibitor and senescence marker p21) were not affected by the presence of IMT1 (Supplementary Fig. 3c). This is in agreement with the well-established concept that inhibition of the SASP does not impair other features of senescent cells, including the inhibition of the cell cycle^{27,28}. Of note, mitochondrial DNA levels were not affected by IMT1 during the 48 h treatment period (Supplementary Fig. 3d, e). To explore the contribution of nuclear-derived dsRNAs to the pool of dsRNAs present in senescent cells, we have focused on repeated retroelements due to their known ability to generate stable dsRNAs²¹. Previous reports have indicated increased expression of retroelements LINE1 and ERVs in senescent cells^{29,30}. We have confirmed these observations in our senescent cells by RT-qPCR (ERVV1, ERV31, LINE1, or ALU elements). However, the majority of the retroelements tested showed no decrease, or even elevation, in their expression following IMT1 treatment (Supplementary Fig. 3c). These observations indicate that mitochondria are the main source of the elevated dsRNA foci present in senescent cells and that mt-dsRNA is an important contributor to the SASP.

Senescent cells are sensitized to dsRNA-dependent innate immune signaling

Nuclear as well as cytosolic dsRNAs are subject to modifications that reduce their pro-inflammatory activity. In particular, the adenosine deaminase ADAR1 is a key RNA modifying enzyme that reduces the capacity of dsRNAs to activate innate immune signaling³¹. Interestingly, compared to proliferative cells, senescent cells presented a marked reduction in the levels of the two ADAR1 isoforms (both

encoded by the same gene *ADAR*)³¹, namely, p150 (which shuttles between nucleus and cytosol) and p110 (mostly nuclear) (Fig. 2a–c; Supplementary Fig. 4a–c). To ascertain whether ADAR1 is functional in senescent cells, despite its lower levels, we treated IMR-90 and SK-MEL-103 cells with siADAR (or scrambled control siSCR) and then we induced senescence. Notably, the presence of siADAR resulted in elevated levels of MAVS, as detected by immunofluorescence (Supplementary Fig. 4d), and in a dramatically enhanced induction of *IFNA1* and *IFNB1* and pro-inflammatory cytokines (Supplementary Fig. 4e). Conversely, we overexpressed each of the two ADAR1 isoforms (p110 or p150) in senescent cells and this led to a reduction in the SASP of senescent IMR-90 cells, while only p150, but not p110 decreased the SASP in senescent SK-MEL-103 cells (Fig. 2d; Supplementary Fig. 4f, g). Together, these observations indicate that senescent cells, by down-regulating ADAR1 protein levels, are hypersensitized to the inflammatory activity of cytosolic dsRNAs.

We then focused on the main cytoplasmic dsRNA sensors. In particular, RIGI (encoded by gene *DDX58*) and MDA5 (encoded by gene *IFIH1*) were upregulated at the mRNA level soon after treatment with senescence-inducing agents (Fig. 2e). This was in contrast to sensors LGP2 (*DHX58*) and PKR (*EIF2AK2*) that remained unchanged in senescent cells (Fig. 2e). The signaling integrator MAVS (MAVS) was significantly upregulated in senescent SK-MEL-103, but not in senescent IMR-90 cells (Fig. 2e). Notably, IMR-90 cells with combined siRNA-mediated depletion of RIGI and MDA5 underwent doxorubicin-induced senescence with reduced expression of cytokines (Fig. 2f; Supplementary Fig. 4h), whereas depletion of PKR did not reduce the expression of the cytokines tested (Supplementary Fig. 4i). In agreement with previous reports^{29,32–34}, combined siRNA-mediated depletion of dsDNA sensor cGAS and STING, followed by induction of senescence, resulted in reduced expression of cytokines (Fig. 2f; Supplementary Fig. 4h). To reinforce the concept that RIGI and MDA5 are involved in the SASP, we measured the presence of a set of cytokines directly in the extracellular medium and confirmed that many

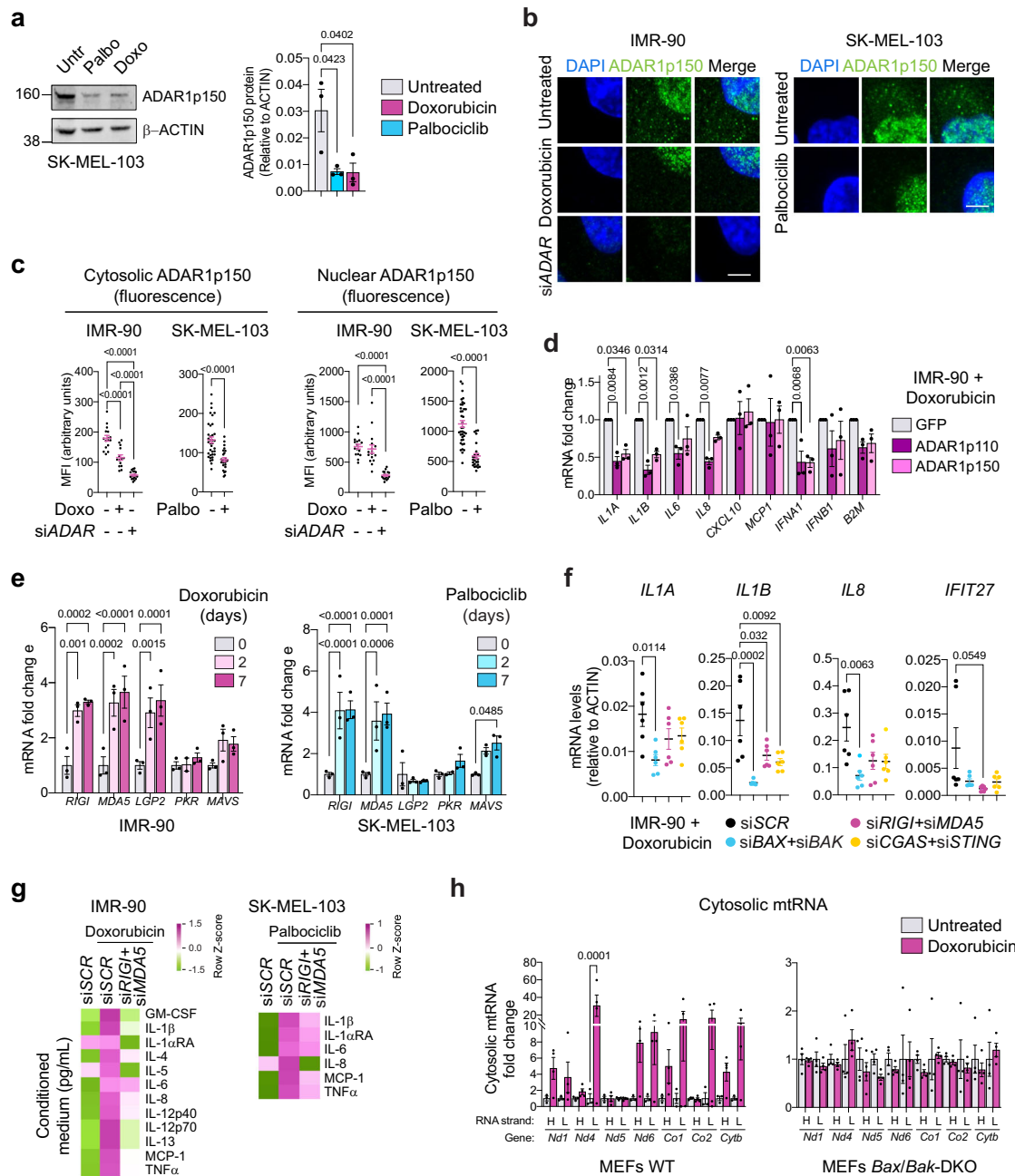


Fig. 2 | Senescent cells are sensitized to dsRNA-dependent innate immune signaling. **a** Western blotting of ADAR1p150 and β-ACTIN expression in untreated and senescent (palbociclib or doxorubicin) SK-MEL-103 cells. Graph quantify ADAR1p150 expression relative to β-ACTIN. **b** Immunofluorescence of ADAR1 in IMR-90 and SK-MEL-103 cells. Representative images are shown. **c** Graphs quantify the mean fluorescence intensity (MFI) of cytosolic and nuclear ADAR1p150 for cells in **(b)**. **d** RT-qPCR analysis of SASP genes in senescent IMR-90 cells transfected with the indicated plasmid. **e** RT-qPCR analysis of different genes after 0 (untreated), 2, 4, or 7 days of senescence induction in IMR-90 or SK-MEL-103 cells exposed to doxorubicin or palbociclib. **f** RT-qPCR analysis of SASP genes in senescent IMR-90 cells treated with the indicated siRNAs. **g** Heat map showing the protein levels of cytokines and chemokines in conditioned media from control or senescent IMR-90 and SK-MEL-103 cells treated with the indicated siRNA, quantified by a multiplex protein assay. Concentration data correspond to a total volume of 2 ml per confluent well of 6-well plates. Z score has been calculated for each protein (row). Green color: under-abundance; magenta color: over-abundance; the

colored scale bar shown at the upper right indicates relative expression values, where -1.5/-1 and 1/1.5 represent under- and over-abundance, respectively. **h** RT-qPCR analysis of mtRNA heavy (H) and light (L) strands in cytosolic fractions of senescent MEFs exposed to doxorubicin. The names of the genes indicate the location of the RNA segment amplified. Data expressed as fold change respect untreated cells. Data show mean ± SEM; mean in **(g)**. Comparisons by one-way ANOVA followed by Tukey's multiple comparisons test for **(a, c)** (IMR-90), **(f)**; two-sided t-test for **(b, c)** (SK-MEL-103); two-way ANOVA followed by Tukey's multiple comparisons test for **(d, e)**; two-way ANOVA followed by Šidák's multiple comparisons test for **(h)**. Exact p-values are shown in all panels. Sample numbers were $n = 3$ independent replicates for **(a)**; $n = 16$ (untreated), $n = 14$ (doxorubicin), $n = 19$ (siADAR) for IMR-90 and $n = 16$ (untreated), $n = 14$ (doxorubicin), $n = 19$ (siADAR) for SK-MEL-103 cells analyzed from 2 to 3 independent replicates for **(b, c)**; $n = 3$ independent replicates for **(d, e)**; $n = 6$ independent replicates for **(f)**; $n = 4$ independent replicates for **(g)**. $n = 4$ independent replicates for **(h)**. Scale bars is 5 μm. Source data are provided as a Source Data file.

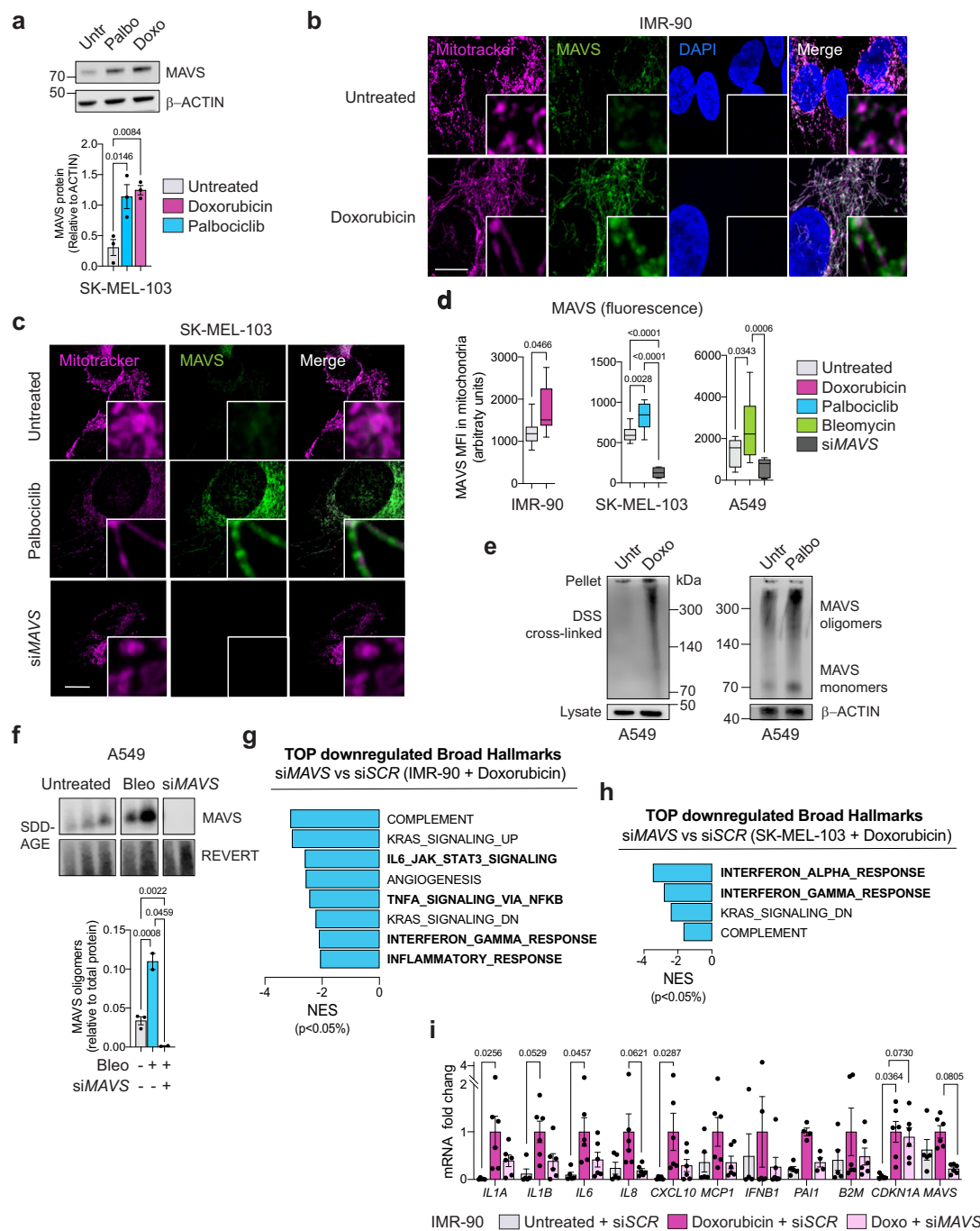


Fig. 3 | Cytosolic mt-dsRNA triggers MAVS-inflammation in cellular senescence to drive the SASP. **a** Western blotting of MAVS and β-ACTIN expression in senescent SK-MEL-103 cells exposed to palbociclib, doxorubicin, or untreated. Graph quantify MAVS expression relative to β-ACTIN. **b, c** Super-resolution AiryScan microscopy images of mitochondria (magenta) and MAVS (green) in senescent IMR-90 cells exposed to doxorubicin or senescent SK-MEL-103 cells exposed to palbociclib, untreated or transfected with siMAVS. **d** Quantification of MAVS mean fluorescence intensity (MFI) in the mitochondrial surface from pictures in **(b, c)** and Supplementary Fig. 5a. **e** DSS cross-linking to study the formation of MAVS oligomers in senescent A549 treated with palbociclib or doxorubicin. **f** SDS-AGE to study the formation of MAVS aggregates in senescent A549 treated with bleomycin. Graph quantify MAVS expression relative to total protein (REVERT). **g, h** Top downregulated Broad Hallmarks from the differential expression analysis (RNA-seq) of siMAVS compared to siSCR senescent IMR-90 or SK-MEL-103 cells exposed to doxorubicin. **i** RT-qPCR of SASP factors in senescent IMR-90

cells exposed to doxorubicin and treated with siMAVS. Untreated and senescent cells transfected with siSCR were used as controls. Data expressed relative to Doxorubicin+siSCR. Data show mean ± SEM; In the box plots in **(d)** the lower and upper boundaries of the box represent the first and third quartiles, with the median indicated by a line inside the box. The whiskers extend to the maximum and minimum values. Comparisons by one-way ANOVA followed by Tukey's multiple comparisons test for **(a, d)** (except two-sided t-test for IMR-90). **(f)**: two-way ANOVA followed by Tukey's multiple comparisons test for **(f)**. Exact p-values are shown in all panels. Sample numbers were $n = 3$ independent replicates for **(a)**; $n = 7$ (untreated, IMR-90), $n = 10$ (doxorubicin, IMR-90), $n = 9$ (untreated, SK-MEL-103), $n = 12$ (palbociclib, SK-MEL-103), $n = 7$ (siMAVS, SK-MEL-103), $n = 11$ (untreated, A549), $n = 15$ (bleomycin, A549), $n = 8$ (siMAVS, A549) fields analyzed from 3 independent experiments for **(d)**; $n = 2$ or 3 independent replicates for **(f)**. $n = 6$ independent replicates for **(i)**. Representative images are shown. Scale bars are 10 μm for **(b)** and 20 μm for **(c)**. Source data are provided as a Source Data file.

the cytokines overproduced upon senescence were normalized upon combined depletion of RIGI and MDA5 (Fig. 2g). In the case of mt-dsDNA, its release from senescent cells involves BAX and BAK⁹. Interestingly, compared to the depletion of RIGI/MDA5 or cGAS/STING, combined depletion of BAX/BAK resulted in a more profound reduction in the expression of SASP-related cytokines (Fig. 2f). The involvement of BAX and BAK in the release of mt-dsRNA in senescent cells was further supported by using mouse embryo fibroblasts doubly-deficient in *Bax* and *Bak* (*Bax/Bak*-DKO). Interestingly, while mtRNA was clearly elevated in the cytosolic fraction of senescent wild-type (WT) MEFs, this was not observed in the cytosolic fraction of senescent *Bax/Bak*-DKO MEFs (Fig. 2h). Accordingly, and consistent with a previous report⁹, IFN-induced genes and SASP factors were reduced in senescent *Bax/Bak*-DKO MEFs treated with doxorubicin compared to senescent WT MEFs (Supplementary Fig. 4j).

In summary, senescent cells downregulate the dsRNA editing machinery and upregulate the dsRNA sensing machinery, together rendering senescent cells highly responsive to cytosolic dsRNA. Our data, together with a previous report⁹, are consistent with a model in which the mitochondria of senescent cells release mt-dsDNAs and mt-dsRNAs to the cytosol in a BAX/BAK-dependent manner, activating the cGAS/STING and RIGI/MDA5 sensors, respectively, triggering inflammatory signaling and the SASP.

MAVS is activated in senescent cells and it is a key inducer of the SASP

The mitochondrial antiviral signaling (MAVS) protein is a signaling hub that integrates multiple inflammatory inputs, most notably those elicited by dsRNA and its sensors RIGI and MDA5²¹. Western blot analysis revealed that MAVS protein levels increased in senescent cells (Fig. 3a). MAVS activation results in large prion-like aggregates in the outer surface of mitochondria detectable by immunofluorescence³⁵. Fluorescence microscopy analysis of MAVS revealed large discrete dots along the mitochondria of senescent IMR-90, SK-MEL-103 and A549 cells (Fig. 3b–d; Supplementary Fig. 5a). This signal was completely lost in senescent cells generated in the presence of a siRNA against *MAVS* mRNA (Fig. 3c, d; Supplementary Fig. 5a). We directly confirmed increased MAVS oligomerization in senescent cells both by disuccinimidyl suberate (DSS) cross-linking followed by acrylamide electrophoresis (Fig. 3e) and by semi-denaturing detergent agarose electrophoresis (SDD-AGE) (Fig. 3f).

To evaluate the impact of MAVS on the transcriptome of senescent cells, we performed RNA-seq in senescent cells (IMR-90 and SK-MEL-103) generated in the presence of si*MAVS* and compared them to senescent cells with scrambled siRNA. Interestingly, among the top downregulated pathways were inflammatory signatures (Broad Hallmarks) (Fig. 3g, h). These observations were confirmed by RT-qPCR; indeed, senescent IMR-90 cells generated in the presence of si*MAVS* were completely devoided of the expression of the tested cytokines and other components of the SASP, such as *PAI1* (also known as *SERPINE1*) and *B2M* (Fig. 3i and Supplementary Fig. 5b). Of note, consistent with the idea that SASP inhibition does not affect other features of senescence, depletion of *MAVS* did not affect the levels of *CDKN1A* (Fig. 3i). We conclude that MAVS aggregation on the outer surface of mitochondria is a distinctive feature of senescent cells and an important mediator of the SASP.

Antagonistic role of mitofusins on the SASP

To better understand the role of mitochondria in senescence, we focused on the fact that senescent cells present highly fused mitochondria⁵ (Fig. 4a), and inhibition of mitochondrial fusion is anti-inflammatory^{36,37}. Based on this, we decided to study the effect of mitofusin inhibition on the SASP. First, we confirmed previous reports indicating that senescent cells present elevated protein levels of mitofusin 1 (MFN1) and mitofusin 2 (MFN2)³⁸ (Supplementary

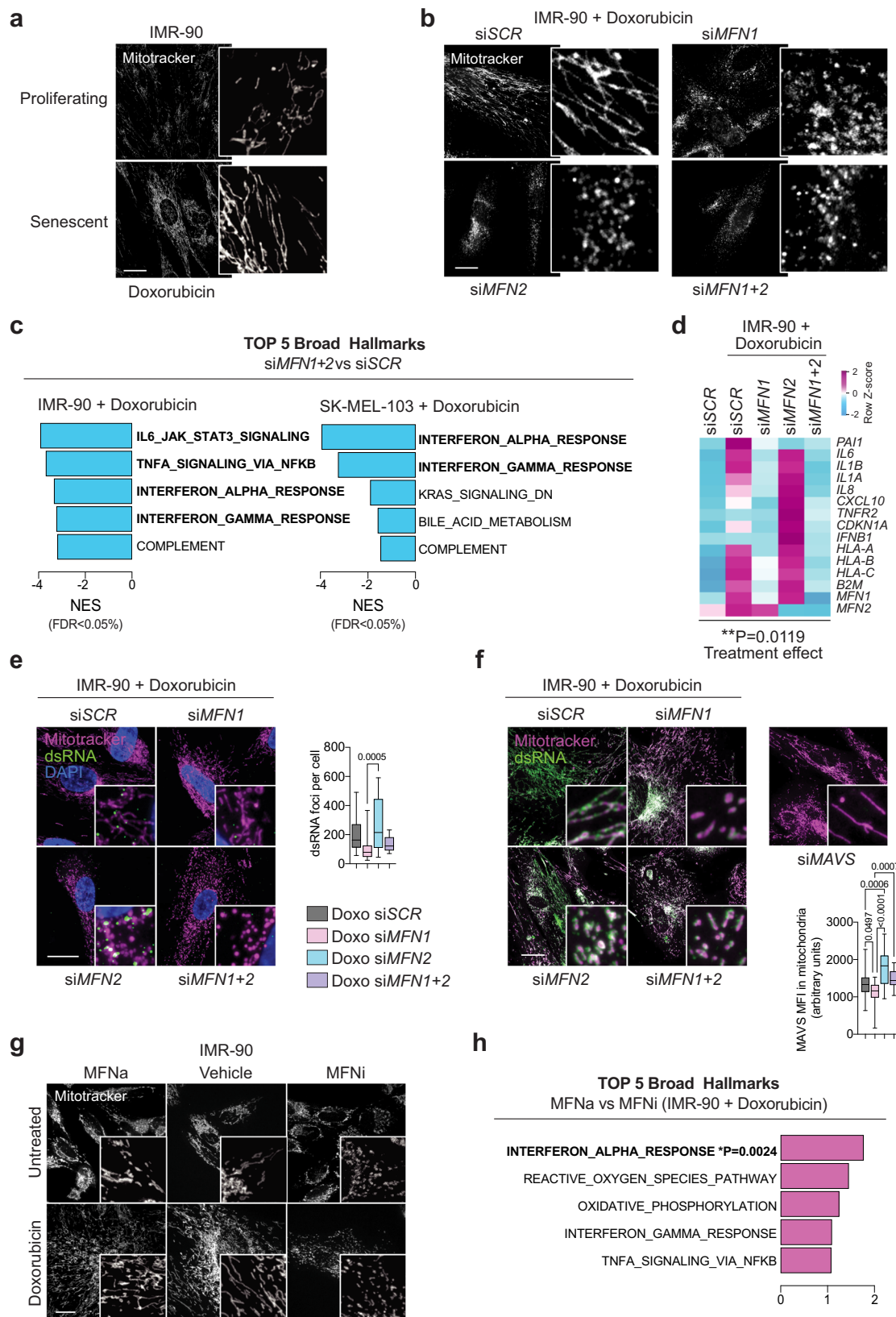
Fig. 6a, b) together with a reduction in the levels of fission-inducing phospho-DRP1(S616)³⁹ (Supplementary Fig. 6c, d). We then downregulated MFN1 and MFN2, alone or combined, by transfecting siRNAs in IMR-90 cells, and this was followed by exposure of cells to doxorubicin to induce senescence. Senescence was allowed to develop for 7 days post-doxorubicin and then we confirmed the downregulation of *MFN1* and *MFN2* (Supplementary Fig. 6e, f). Downregulation of mitofusins, alone or combined, caused fragmentation of mitochondria, although fragmentation was much more extensive in the case of si*MFN2* compared to si*MFN1* in the three cell lines tested (IMR-90, SK-MEL-103 and A549) (Fig. 4b; Supplementary Fig. 6g). Importantly, mitochondria fragmentation did not affect the development of senescence features such as SABG staining (Supplementary Fig. 6h). Gene set enrichment analysis (GSEA) of the transcriptome of senescent IMR-90 and SK-MEL-103 cells with combined inhibition of MFN1 and MFN2 (si*MFN1+2*) revealed cytokine and interferon signaling among the most downregulated signatures (Fig. 4c). These results were validated by RT-qPCR analysis. In particular, we focused on cytokines characteristic of the SASP and IFN-signaling targets related to the MHC-I^{40,41}, both of which were significantly downregulated compared to senescent cells treated with scrambled siRNA (Fig. 4d; Supplementary Fig. 6i, j).

Recent reports have uncovered a complex interplay between MFN1 and MFN2 in relation to MAVS and inflammation. In particular, although the combined inhibition of the two mitofusins is anti-inflammatory^{36,37}, this is not the case for their single inhibition: single downregulation of MFN1 is anti-inflammatory⁴², whereas single downregulation of MFN2 is pro-inflammatory^{43,44}. The mechanistic basis for these differential effects on inflammation remains to be elucidated; but the fact that the combined inhibition has the same phenotype as single MFN1 inhibition suggests that MFN1 acts downstream of MFN2. We observed the same pattern in relation to the SASP of senescent IMR-90 cells: si*MFN1* significantly decreased the SASP and IFN responsive genes; si*MFN2* further elevated the expression of these genes; and combined inhibition of both mitofusins recapitulated the same effect as the inhibition of MFN1 alone (Fig. 4d). It is interesting to note that, while both si*MFN1* and si*MFN2* induce mitochondrial fragmentation, only si*MFN1* suppresses the SASP, thus disconnecting fragmentation from inflammation. In an effort to further characterize the role of mitofusins in senescence-driven inflammation, we observed that si*MFN1* strongly reduced the amount of dsRNA (J2) foci and MAVS aggregates, while si*MFN2* elevated the amount of both of them (Fig. 4e,f; Supplementary Fig. 7a–c). In fact, si*MFN1* reduces the levels of pIRF3 and RIGI, both of which are increased in senescent cells (Supplementary Fig. 7d). Moreover, the individual mRNA levels of *IL6*, *IL1A*, *IFNA1*, and protein levels of HLA-A/B/C determined by cytometry were positively correlated with the levels of dsRNA (J2) foci and mitochondrial MAVS aggregates (Supplementary Fig. 7e, f).

These observations indicate that mitofusins modulate the levels of mt-dsRNA foci in senescent cells in an antagonistic manner, with the inhibition of MFN1 being dominant and anti-inflammatory.

Pharmacologic inhibition of mitofusins reduces the SASP

Building upon the finding that combined depletion of mitofusins leads to a reduction in the SASP, we aimed to achieve similar results using pharmacological tools. We have recently reported small molecules rationally designed to destabilize or stabilize the anti-tethering, non-fusogenic, conformation of mitofusins⁴⁵. In particular, compound MASM7 (abbreviated here as MFNa) activates both MFN1 and MFN2, whereas compound MFI8 (abbreviated as MFNi) inhibits both mitofusins⁴⁵. Senescence was induced for 7 days in IMR-90 and SK-MEL-103 cells and then they were treated with MFNa or MFNi for 48 h. As expected, MFNi induced fragmentation, both in senescent and proliferative IMR-90 and SK-MEL-103 cells (Fig. 4g; Supplementary Fig. 8a, b). Senescent cells present high basal levels of fusion and,



therefore, treatment with MFNa only modestly increased fusion (Supplementary Fig. 8b). At the drug concentrations used, we did not observe cell death after a period of 48 h (Supplementary Fig. 8c). To capture the transcriptional programs most sensitive to pharmacological activation or inhibition of mitofusins, we compared the transcriptome of senescent IMR-90 cells treated for 48 h with MFNa or

MFNi. Although only a limited number of pathways presented enrichment in MFNa-treated compared to MFNi-treated senescent cells, the elevation of IFN targets emerged as a significant upregulated Broad Hallmark (Fig. 4h). Moreover, analysis by RT-qPCR confirmed the inhibition of SASP factors upon treatment with MFNi in senescent SK-MEL-103 and A549 cancer cells (Supplementary Fig. 8d, e). The

Fig. 4 | Antagonistic role of mitofusins on mt-dsRNA/MAVS activation in senescent cells. **a** Super-resolution AiryScan microscopy images. Mitochondria were visualized by live-cell imaging in IMR-90, untreated or exposed to doxorubicin. Mitochondria were stained with mitotracker. **b** Super-resolution AiryScan microscopy images. Mitochondria were visualized by live-cell imaging using mitotracker in senescent IMR-90 cells induced with doxorubicin in the presence of the indicated siRNA. **c** Top downregulated Broad Hallmarks from the differential expression analysis (RNA-seq) of senescent IMR-90 or SK-MEL-103 exposed to doxorubicin in the presence of siMFN1+2. Senescent cells transfected with siSCR were used as control. **d** Heatmaps showing the alteration in SASP factors. Senescence was induced in IMR-90 cells by doxorubicin in the presence of the indicated siRNA. Untreated cells transfected with siSCR were used as control. Data was generated measuring mRNA levels by qPCR and normalized to *B-ACTIN* from 4 independent replicates and Z score has been calculated for each gene (row). Blue color: under-abundance; magenta color: over-abundance; the colored scale bar shown at the upper right indicates relative expression values, where -2 and 2 represent under- and over-abundance, respectively. **e** Immunostaining of dsRNA (green) in senescent IMR-90 cells treated with doxorubicin and the indicated siRNA. Mitochondria (magenta) and nuclei (blue) were stained with MitoTracker and DAPI, respectively. Graph quantify dsRNA foci per cell. **f** Immunostaining of MAVS (green)

in senescent IMR-90 cells exposed to doxorubicin in the presence of the indicated siRNA. Mitochondria (magenta) were stained with MitoTracker. Graph quantify MAVS mean fluorescence intensity (MFI) in the mitochondrial surface. **g** Spinning disk confocal images of control (untreated) and senescent IMR-90 cells treated with MFNa (mitofusin activator MASM7) or MFNi (mitofusin inhibitor MFI8) for 6 h. Mitochondria were stained with mitotracker. **h** Top upregulated Broad Hallmarks from the differential expression analysis (RNA-seq) of senescent IMR-90 treated with MFNa compared to MFNi. Only IFN- α presented statistical significance ($P = 0.0024$). In the box plots, the lower and upper boundaries of the box represent the first and third quartiles, with the median indicated by a line inside the box. The whiskers extend to the maximum and minimum values. Comparisons by two-way ANOVA for **(d)** revealed a significant main effect of the treatment factor ($F(4, 156) = 3333, P = 0.0119$); one-way ANOVA followed by Tukey's multiple comparisons test for **(e, f)**. Exact p -values are shown in all panels. Sample numbers were $n = 3$ independent replicates analyzed in **(c, d, and h)**; $n = 15$ (siSCR), $n = 23$ (siMFN1), $n = 24$ (siMFN2), $n = 6$ (siMFN1+2) cells analyzed from 3 independent experiments for **(e)**; $n = 22$ (siSCR), $n = 22$ (siMFN1), $n = 24$ (siMFN2), $n = 23$ (siMFN1 + 2) cells analyzed from 4 independent experiments for **(f)**; The z projections of representative images are shown. Scale bars are all 20 μm . Source data are provided as a Source Data file.

extracellular medium of senescent cells treated with MFNi also presented decreased concentration at the protein level of those SASP factors (Supplementary Fig. 8f). These observations support the idea that it is possible to suppress the SASP of senescent cells by pharmacological inhibition of MFN1.

mt-dsRNA accumulates in senescent cells in vivo

Finally, we aimed to extend our results on the mt-dsRNA/MAVS/SASP axis to cellular senescence in *in vivo* contexts. We began by examining xenografts of human SK-MEL-103 cells grown in nude mice and treated with palbociclib, which efficiently induces senescence *in vivo*⁴⁶. Foci of dsRNA (J2) were clearly detected in histological sections of palbociclib-treated tumors, but not in untreated tumors (Fig. 5a; Supplementary Fig. 9a). We then focused on fibrotic lesions because of their strong association with senescent cells⁴⁷. We directed our attention towards the heart and used a mouse model of myocardial ischemia by permanently blocking the left anterior descending (LAD) coronary artery, which closely mimics the pathophysiology of myocardial infarction. As expected⁴⁸, one week after heart ischemia, there was a significant increase in collagen deposition, iron levels, p21, and SABG-positive cells in the infarcted tissue (Supplementary Fig. 9b). Interestingly, we observed a significant increase in dsRNA levels detected by the J2 antibody in infarcted hearts (Fig. 5b), and a positive correlation between the individual levels of SABG and dsRNA (J2) per infarcted heart analyzed (Fig. 5c).

Multiple studies have demonstrated that senescent cells accumulate during aging⁴⁹. We therefore analyzed SABG activity and dsRNA in tissues from young and aged mice. We observed an accumulation of dsRNA (J2) in the brain and liver sections of old mice compared to young mice, and the total levels observed per mouse sample correlated with the total levels of SABG (Fig. 5d; Supplementary Fig. 9c, d). We also detected increased expression of mRNAs from both H and L strands in the brain of old mice (Supplementary Fig. 9e), supporting an accumulation of mt-dsRNA with aging. Importantly, when we analyzed histological sections of the liver and kidney, we observed a good colocalization between areas with dsRNA (J2) accumulation and SABG positivity (Fig. 5e; Supplementary Fig. 9f). These results are consistent with the elevated expression of type I interferon response genes, p16 (*Cdkn2a*) and dsRNA sensors in old mice across different tissues (Fig. 5f).

To gain insight into the potential implications in humans, we examined the expression of dsRNA sensors and mitochondrial genes in a publicly available dataset of healthy volunteers at different ages⁵⁰. Interestingly, the levels of the pro-inflammatory genes *RIGI*

(*DDX58*), *MDAS* (*IFIH1*) and *MAVS* clearly increased with aging, while the anti-inflammatory genes *ADAR* and *ADARB1* decreased with age (Fig. 5g). We also observed an upregulation of mitochondrial-encoded genes (*MT-ND1* and *MT-ATP8*), while nuclear-encoded mitochondrial genes (*SDHA*, *ATPSAI*) did not increase (Fig. 5g). Sensors for dsDNA *CGAS*, *STING* or *TLR9* also increased with age. These expression patterns are reminiscent of senescent cells. As additional supportive data, mitochondrial mRNA transcripts circulating in a cell-free form in the serum are among the most significantly elevated during aging in humans⁵¹ (Fig. 5h).

Finally, to establish a direct association between dsRNA foci and senescence *in vivo*, we treated old mice with the senolytic drug navitoclax for 14 days. This regimen of navitoclax efficiently reduces the burden of senescent cells in the kidney (Supplementary Fig. 9g). We observed that senescent cell removal in the kidney also caused a reduction in dsRNA (J2) foci (Supplementary Fig. 9h). To reinforce the *in vivo* link between mt-dsRNA and inflammation, we induced systemic senescence in mice by treatment with doxorubicin. As expected, doxorubicin significantly increased the serum levels of many cytokines. Interestingly, however, concomitant treatment with doxorubicin and IMT1 attenuated the systemic inflammatory response *in vivo* (Fig. 5i). These observations provide *in vivo* evidence of the link between mt-dsRNA and senescence-associated inflammation.

Discussion

Here, we provide evidence that mt-dsRNA is released during cellular senescence by different cell types, non-cancerous and cancerous, and in response to different types of triggers, including genotoxic agents such as doxorubicin, inhibitors of cyclin-dependent kinases, such as palbociclib, and replicative senescence. We observed an increase in dsRNA foci *in vivo* in tumors treated with chemotherapeutic agents, in fibrotic lesions associated with cellular senescence, such as post-infarction heart, and also in aged tissues, such as liver, brain, and kidney. We have found suggestive colocalization of dsRNA foci and the senescence marker senescence-associated β -galactosidase (SABG) in the kidney and liver of old mice. Moreover, treatment of old mice with the senolytic agent navitoclax reduced the detection of dsRNA, thereby linking *in vivo* the presence of dsRNA and senescence. Importantly, we show that a highly selective inhibitor of the mitochondrial RNA polymerase, IMT1, almost completely abrogates the detection of dsRNA foci in senescent cells, and strongly reduces the senescence-associated secretory phenotype (SASP), both *in vitro* and *in vivo*. IMT1 does not affect the expression levels of retroelements that could conceivably contribute to the formation of dsRNAs^{52,53}.

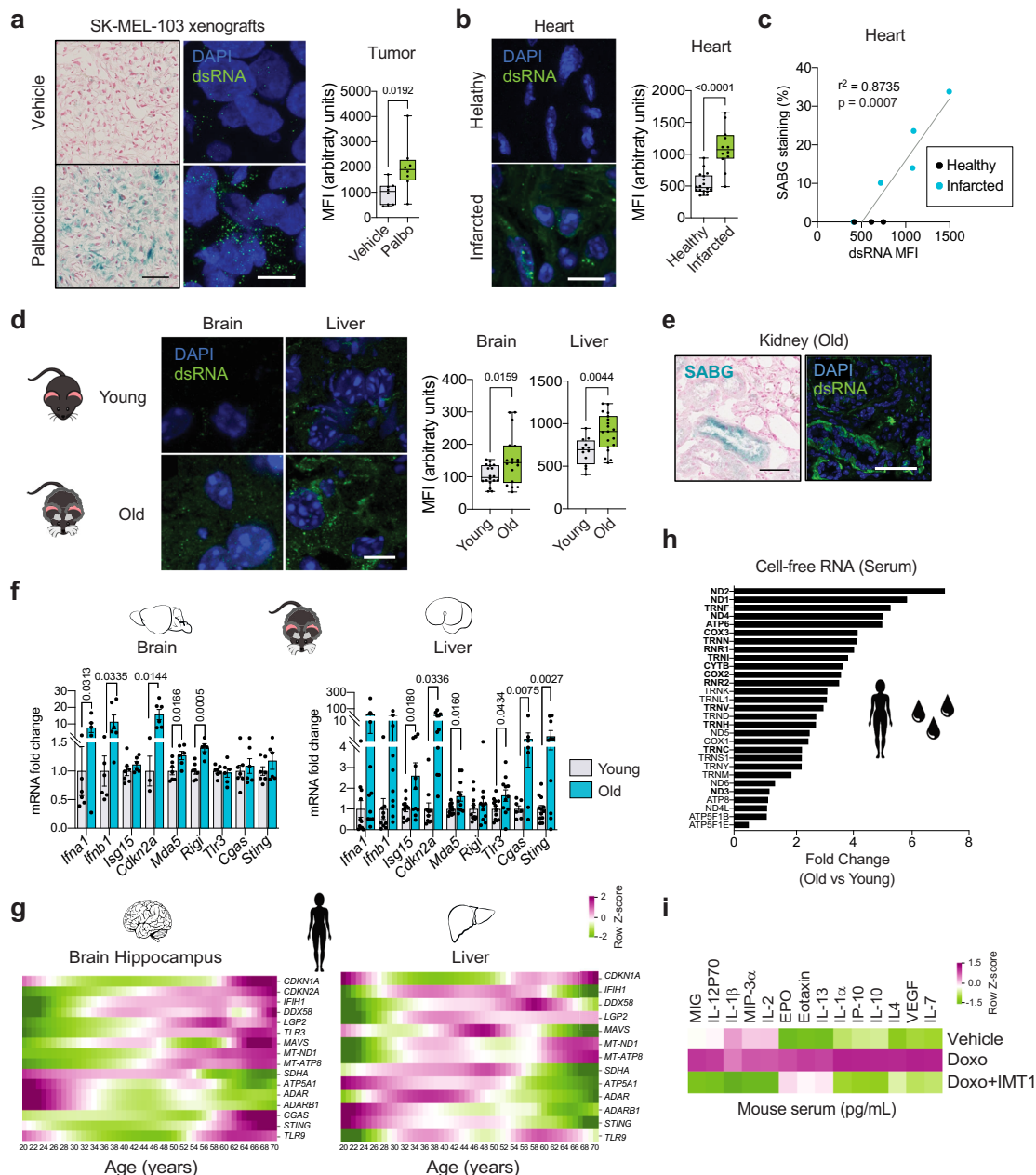


Fig. 5 | mt-dsRNA accumulates in senescent cells in vivo. **a** A SABG staining and dsRNA immunofluorescence staining in tumor sections from mice treated with palbociclib or vehicle. Nuclei are stained with nuclear fast red or DAPI. Graph quantify dsRNA mean fluorescence intensity (MFI). **b** Fluorescence immunohistochemistry staining of dsRNA (J2) in healthy and infarcted mouse hearts. Nuclei are stained with DAPI. Graph quantify dsRNA mean fluorescence intensity (MFI). **c** Correlation plot between SABG staining and dsRNA mean fluorescence intensity (MFI) in the mouse heart. **d** Fluorescence immunohistochemistry staining of dsRNA (J2) in brain and liver sections from young (2–3 months) and old (20–28 months) mice. Nuclei are stained with DAPI. Graph quantify dsRNA mean fluorescence intensity (MFI). **e** SABG staining and dsRNA immunofluorescence staining in kidney sections from old mice. **f** RT-qPCR analysis of different genes in the brain and liver of young (2–3 months) and old (20–28 months) mice. **g** RNA expression in human tissues. Z score has been calculated for each gene (column). The colored scale bar shown at the upper right indicates relative expression values, where -2 (green) and 2 (magenta) represent under- and over-abundance, respectively. **h** Mitochondrial-encoded gene transcripts present

in serum cell-free-RNA. Fold change between old (80–85 years) versus young (30–32 years) individuals are represented for each gene. Bold indicates significantly upregulated transcripts ($P < 0.05$). **i**. Cytokines levels in the serum from mice treated with the indicated drugs. In the box plots in (a, b, d), the lower and upper boundaries of the box represent the first and third quartiles, with the median indicated by a line inside the box. The whiskers extend to the maximum and minimum values; mean \pm SEM in (f); mean in (g–i). Comparisons by two-sided t -test for (a, b, d); multiple t -test for (f). Exact p -values are shown in all panels. Sample number were 3 randomly sampled regions in $n = 2$ (vehicle) and $n = 2$ (palbociclib) mice in (a); 3 randomly sampled regions in $n = 4$ (healthy) and $n = 4$ (infarcted) mice in (b); each dot represents the mean of $n = 3$ replicates in (c); 3 randomly sampled regions in $n = 4$ (young) and $n = 5$ (old) mice for brain, $n = 4$ (young) and $n = 6$ (old) mice for liver in (d); $n = 7$ (young) and $n = 6$ (old) mice for brain, $n = 11$ (young) and $n = 12$ (old) mice for liver from 2 independent cohorts in (f). Representative images are shown. Scale bars are 50 μ m (SABG) and 10 μ m (dsRNA) for (a), 10 μ m for (b–d), 125 μ m (SABG) and 50 μ m (dsRNA) for (e). Source data are provided as a Source Data file.

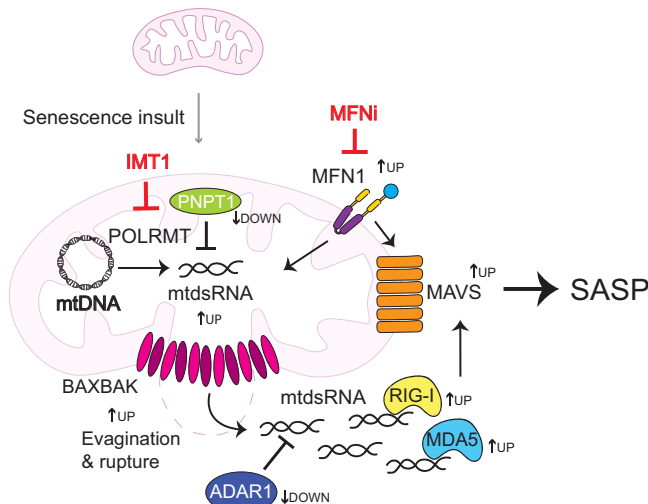


Fig. 6 | Model summarizing the main findings of this work. In senescent cells, mt-dsRNA accumulation is enhanced by PNPT1 downregulation, and its leakage into the cytoplasm is favored by mitochondrial membrane budding structures and rupture, releasing mt-dsRNA into the cytosol in a process that requires BAX and BAK. ADAR1 downregulation favors mt-dsRNA recognition by MDA5 and RIG-I sensors, activating the MAVS signaling pathway and SASP expression. MFNI acts as an activator of this pathway by modulating mt-dsRNA formation and MAVS activation. Pharmacological inhibition of this pathway with IMT1 (POLRMT inhibitor) and MFNI (mitofusins inhibitor) attenuates the SASP.

Indeed, a small fraction of dsRNA foci (~10%) persist in senescent cells after IMT1 treatment and they could correspond to non-mitochondrial dsRNA sources, such as transcribed retroelements. Together, all the above evidence directly involve mt-dsRNA as the primary source of dsRNA in senescent cells and as a key inducer of the SASP (Fig. 6).

The inflammatory genetic syndromes Aicardi-Goutières and Leigh are associated with mutations in *PNPT1* and *ADAR1*^{20,25}. Interestingly, these two genes are functionally connected to mt-dsRNA. *PNPT1* is critical for preventing the accumulation of mt-dsRNA¹⁵ and *ADAR1* edits dsRNA, including mt-dsRNA, to reduce its inflammatory activity^{15,31}. Interestingly, we have observed that senescent cells are characterized by very low protein levels of *PNPT1* and *ADAR1*, which makes them prone to accumulate and release inflammatory mt-dsRNA. In the case of cells lacking *PNPT1* or undergoing caspase-independent cell death, mt-dsRNA escapes from mitochondria through BAX/BAK pores^{15,34}. BAX/BAK pores are also responsible, at least in part, for the escape of mt-dsDNA from the mitochondria of senescent cells⁹. We have found that the depletion of BAX/BAK in senescent cells strongly reduces the SASP and this effect is more pronounced than the depletion of the dsDNA sensors cGAS/STING or the dsRNA sensors RIGI/MDA5. This suggests a scenario in which the mitochondria of senescent cells release two critical inflammatory signals through BAX/BAK pores, namely, mt-dsDNA and mt-dsRNA. Moreover, we have found that senescent cells upregulate the two main dsRNA sensors involved in the activation of inflammation RIGI and MDA5. In summary, our findings suggest that the downregulation of *PNPT1* and *ADAR1*, together with the upregulation of RIGI and MDA5, render senescent cells extremely prone to the inflammatory activity of mt-dsRNA (Fig. 6).

Mitofusins interact with MAVS and regulate inflammation in opposite directions^{42,43}. In our work, we build on these concepts to expand their relevance to cellular senescence. Specifically, we found that MFNI elimination reduces the levels of dsRNA, inhibits the formation of active MAVS aggregates, and impairs the SASP, while MFN2 elimination has the opposite effect. We also show that the effect of MFN1 depletion on the mt-dsRNA/MAVS axis is dominant

over MFN2 depletion, as the double depletion of MFN1+2 recapitulates the same effects as single MFN1 elimination. Importantly, recently developed small molecules that directly inhibit both mitofusins⁴⁵ are able to reduce SASP expression (Fig. 6). This approach could have potential implications for developing novel interventions to mitigate the deleterious effects of senescence in various disease contexts.

In conclusion, we identify the release of mitochondrial dsRNA as an important mediator of the SASP in senescent cells. Additionally, we demonstrate that the pharmacological elimination of mt-dsRNA or inhibition of mitofusins is efficient in attenuating the SASP. Understanding these molecular pathways opens up new possibilities for targeted interventions to counteract cellular senescence and improve treatment outcomes in aging-related pathologies.

Methods

Animal experimentation

Mouse procedures. Male and female C57BL/6 mice between 2 and 4 months were used. For aging studies, male and female C57BL/6 mice between 2 and 3 months were used as young, and between 20 and 28 months were used as old. Animals had *ad-libitum* access to food (SAFE® A40) and water throughout the study period and maintained in a 12 h–12 h light-dark cycle. All animals were housed under specific pathogen-free conditions in the mouse facility of the Institute for Research in Biomedicine (IRB) in accordance with the protocols approved by the Animal Care and Use Ethical Committee of animal experimentation of the Barcelona Science Park (CEEA-PCB) and the Catalan Government. Euthanasia of animals was performed by CO₂.

Ischemic heart fibrosis. Three-four months old male C57BL/6J mice were used. Intraoperative analgesia was induced by treating mice with buprenorphine (0.1 mg/kg) 60 min prior to anesthesia. Anesthesia was induced with 5% isoflurane and it was maintained at 2% with mechanical ventilation following endotracheal intubation (2% isoflurane/97% oxygen, 130–140 stroke rate, stroke volume initially 5 ml/kg-increased to 7.5 ml/kg post-thoracotomy). Animals were placed on a heating table during the whole surgery and eyes were covered with ophthalmic gel (LACRYVISC 3 mg/g, Alcon) to protect the corneas. Neck hair and hair in the upper thorax were removed using a depilatory cream. An incision was made, followed by a left-sided thoracotomy at the fourth intercostal space. The pericardium was removed and the heart left anterior descending artery was located between the pulmonary artery and the left auricle and was ligated using an 8-0 Prolene suture (PremiCron®- B Braun Surgical, S.A.). The thoracic incision was closed in layers, using 6-0 Prolene sutures (PremiCron®- B Braun Surgical, S.A.) to adapt the ribs and 4-0 Prolene sutures (PremiCron®- B Braun Surgical, S.A.) to close the skin. A heating lamp was used to warm the animals until they fully recovered from the anesthesia. Analgesic treatment continued during the 3 following days after surgery by intraperitoneal injections of buprenorphine every 12 h. Sham-operated mice were used as control.

SK-MEL-103 xenograft tumors. 2×10^5 SK-MEL-103 cells were harvested, resuspended in a mixture of PBS and matrigel (1:1), and subcutaneously injected in the flank of athymic nude female mice of 8–12 weeks. Once tumors were visible, approximately at day 7, the mice were randomly assigned to the palbociclib-treated group, which received 100 mg/kg of palbociclib by oral gavage in 50 mM sodium lactate every day, or the control group, which received vehicle. Mice were treated for 8 days. Tumor growth was monitored by caliper measurements and tumor volume was calculated using the formula volume = (length * width²) / 2. The tumors were then extracted and frozen in OCT for SABG or dsRNA staining as described below.

Analysis of cytokines in mouse serum. Two-months old immunocompetent C57BL/6J male and female mice, with a subcutaneous tumor by injection of B16-F10 cells one week before the treatment, were used. One week later, animals were randomly assigned to the doxorubicin-treated group, which received 50 mg/kg of doxorubicin intraperitoneally dissolved in water (day 0 and 3), or the control group, which received vehicle. Starting at day 0, mice were treated with IMT1 (100 mg/kg) or vehicle (10% DMSO, 40% PEG300, 5% Tween 80, 45% saline) by oral gavage until day 7. On day 7, mouse serum was extracted, centrifuged at 2000 × g for 10 min at 4 °C, and then stored at -80 °C. Levels of cytokines, chemokines, and other factors were quantified using Mouse Cytokine/Chemokine 44-Plex Discovery Assay Array (MD44) (Eve Technologies Corporation, Canada).

Senolytic treatment in vivo. Old C57BL/6J male and female mice between 20 and 28 months were treated with navitoclax once daily for 2 weeks by oral gavage (50 mg/kg/day). Control mice were treated with vehicle (10% DMSO, 30% PEG400, 60% PHOSAL®PG).

Cell culture treatments

Cell lines. SK-MEL-103 (human melanoma), IMR-90 (human fetal lung fibroblast), A549 (human non-small cell lung cancer), and B16-F10 (mouse melanoma) were obtained from ATCC. Human foreskin fibroblasts were kindly provided by K. Raj (Altos Laboratories). Wild-type (WT) mouse embryonic fibroblasts (MEFs) were isolated from 13.5-day C57BL/6J mouse embryos. MEFs *Bax/Bak*-DKO were obtained from ATCC. Cells were cultured in standard DMEM supplemented with 10% heat-inactivated Fetal Bovine serum (FBS) (Gibco) and 1% antibiotics (penicillin/streptomycin 100 U/mL; (Gibco)). Cells were maintained in a humidified incubator at 37 °C and 5% CO₂. IMR-90 cells were cultured under 2% O₂. Cells were routinely tested for mycoplasma contamination using standard PCR, and only negative cells were used.

Senescence induction in vitro. Cells were plated subconfluent and cultured in the presence of 1 μM palbociclib (PD033299, Pfizer Inc.), 200 nM doxorubicin (D1515, Sigma), or 10mU/ml bleomycin (B8416, Sigma) for 2 days, after which cells were washed, and replenished with complete culture medium. Palbociclib was added to the medium with every replenishment. To induce senescence by irradiation, cells were plated subconfluent and exposed to a dose of 20 Gy irradiation. Seven days after the treatment (unless specified), senescent cells were collected and used for experiments.

Small molecules treatments. Experiments for in vitro assays were performed after senescence induction unless indicated elsewhere, with the addition of IMT1 (0.1–1 μM, 48 h), MFI8 (20 μM, 48 h) or MASM7 (10 μM, 48 h). PCR, western blot, immunostaining, and SABC assay were performed immediately after treatments.

siRNAs transfection. siRNA pools (siPOOLS) with a complexity of 30 optimally-designed siRNAs were acquired from siTOOLs Biotech GmbH. siRNA gene knock-down was performed on untreated cells. One day after transfection, senescence was induced for 7 days as described above. Lipofectamine reagent (RNAiMAX; Cat. 13778075) was diluted in Opti-MEM (Cat. 31985062) and used according to the manufacturer's instructions.

Conditioned medium analysis. Cells were cultured in DMEM medium under standard conditions. Forty-eight hours before medium collection, cells were incubated in the presence of MFI8 or MASM7 as described above. For cells transfected with siRNA, the medium was changed 48 h before collection without any treatment. Conditioned medium (CM) was collected, centrifuged at 3000 × g, and then stored at -80 °C. Levels of cytokines, chemokines, and other factors were

quantified using the Human Cytokine 15-Plex Discovery Assay Array (HDF15) and Human Interferon 9-Plex Discovery Assay Array (HDIFN9) (Eve Technologies Corporation, Canada).

Cell viability assay

To measure cell survival after treatment with mitofusin activator (MFNa; 20 μM, 48 h) and inhibitor (MFNi; 20 μM, 48), we used CellTiter-Glo® Luminescent Cell Viability Assay (Promega).

Separation of cytoplasmic and mitochondrial fractions

Cytoplasmic and mitochondrial fractions were prepared using the Mitochondria Isolation Kit (89874, Thermo Fisher Scientific). The purity of fractions was tested by western blot according to standard protocols. RNA was extracted using RNeasy Mini Kit (Qiagen) with DNase on-column treatment.

Western blotting

Cell pellets were lysed in 50 mM Tris-HCl pH8; 1 mM EDTA; 150 mM NaCl; 1% NP40; 0.5% Triton X-100; 1.0% SDS, with freshly added protease inhibitors (87785, Thermo Fisher) and phosphatase inhibitors (4906837001, Roche). A total protein of 15 or 30 μg was run on NuPAGE 4–12% gradient Bis-Tris gels and transferred to 0.2 μm nitrocellulose membranes (10600001, GE Healthcare). Blots were blocked with a LICOR blocking buffer and incubated with the corresponding antibodies. β-ACTIN was used as a loading control. Revert™ 700 Total Protein Stain (962-11011, LICORbio) was used to normalize to total protein. Antibodies used are in Supplementary Table 1.

MAVS oligomerization assay

SDD-AGE. For semi-denaturing detergent agarose electrophoresis (SDD-AGE), cells were harvested on day 7 after senescence induction, then washed twice with PBS, resuspended in 1× sample buffer (0.5 × TBE, 10% glycerol, 2%SDS, and 0.0025% bromophenol blue), incubated for 5 min and loaded onto a 1.5% agarose gel. After electrophoresis in the running buffer (1× TBE and 0.1% SDS) for 45 min with a constant voltage of 100 V at 4 °C, the proteins were transferred overnight at 20 V for immunoblotting.

DSS cross-linking

For dissuccinimidyl suberate (DSS) cross-linking followed by acrylamide electrophoresis, cells were harvested at day 7 after senescence induction, then washed twice with PBS before being lysed in CHAPS buffer (10 mM HEPES pH 7.4, 150 mM NaCl, 1% CHAPS) with phosphatase inhibitor cocktail (Thermo Fisher #78440) and incubated for 30 min at 4 °C. Samples were then centrifuged for 10 min at 6000 × g. The pellet was washed once with HEPES 50 mM with a phosphatase inhibitor cocktail and then centrifuged for 10 min at maximum speed. The pellet was crosslinked with 500 μl buffer (HEPES 50 mM, 150 mM NaCl), phosphatase inhibitor cocktail, disuccinimidyl suberate (DSS) (at 2 mM final concentration). Samples were vortexed and incubated for 45 min in a 37 °C, 600 rpm heat block-shaker. Tris-HCl (pH 7.5) (at 20 mM final concentration) was added for 15 min to quench the reaction. Samples were centrifuged for 15 min at 4 °C, maximum speed. The resulting pellet was resuspended in 1× Laemmli sample buffer (with 5% β-mercaptoethanol) and subsequently boiled for 5 min at 95 °C before being run on a SDS-PAGE Bis-Tris 4–12% NuPage gel (Thermo Fisher Scientific). The primary antibody anti-MAVS used was Santa Cruz sc-166583.

Flow cytometry

For analysis of cultured cell lines, cells were digested into single cells by trypsinization (0.25% trypsin-EDTA, Invitrogen). To assess mitochondrial mass, cells were previously treated with MitoTracker™ Red CMXRos (7512, Thermo Fisher) at 200 nM for 30 min at 37 °C. For HLA/B/C detection, cells were trypsinized, washed with PBS, and then

incubated with anti-mouse CD16/CD32 at 1:400 (BD Fc BlockTM, BD Biosciences #553142) for 10 min at 4 °C in FACS Buffer. Then, cells were washed and incubated with antibodies in Supplementary Table 2 for 30 min at 4 °C. Cell viability was assessed using DAPI (0.1 µmol/L, Molecular Probes, #D1306) following the manufacturer's instructions. Dead cells were excluded from the analysis. Cell suspensions were run on a FACSAria™ Fusion Cell Sorter (BD Biosciences). Autofluorescence signal from the unstained samples was obtained and subtracted from each sample in all experiments. Data were analyzed using FlowJo v10 software.

RT-qPCR: RNA extraction, cDNA synthesis and PCR

Total RNA was isolated from cell pellets or tissue using the Trizol (Invitrogen) or the RNeasy® Micro Kit (Qiagen) and cDNA was synthesized using the iScript™ Advanced cDNA Synthesis Kit (BIO-RAD). qPCR was performed on the QuantStudio6K (Thermo Scientific) using the GoTaq, qPCR Master Mix (Promega), and specific primers. Thermocycling conditions were as follows: initial step of 10 min at 95 °C, then 40 cycles of 15 s denaturation at 95 °C, 1 min annealing at 60 °C and 15 s extension at 72 °C. Reactions were run in triplicate, and normalization of all the qRT-PCR data was done by the 2- $\Delta\Delta$ Ct method (Yuan et al. 2006) using the housekeeping genes *B-ACTIN* and *GAPDH* as endogenous controls. The primers used are in Supplementary Tables 3 and 4.

RNA-seq library preparation, sequencing, and bioinformatic analysis

Total RNA was extracted using the RNeasy® Mini Kit (Qiagen), following the manufacturer's instructions.

Library preparation and sequencing. RNA extractions were quantified with a Nanodrop One (Thermo Fisher), and RNA integrity was assessed using the RNA ScreenTape assay of the Tapestation 4200 platform (Agilent). The integrity of a restricted subset of samples was reconfirmed with the Bioanalyzer 2100 RNA Nano assay (Agilent). Libraries for RNA-seq were prepared at IRB Barcelona Functional Genomics Core Facility. Briefly, mRNA was isolated from 760 ng of total RNA and used to generate dual-indexed cDNA libraries with the Illumina Stranded mRNA ligation kit (Illumina) and UD Indexes Set A (Illumina). Ten cycles of PCR amplification were applied to all libraries. Sequencing-ready libraries were quantified using the Qubit dsDNA HS assay (Invitrogen) and quality controlled with the Tapestation HS D5000 assay (Agilent). Three equimolar pools were prepared with the sixty libraries and submitted for sequencing at the *Centro Nacional de Análisis Genómico* (CNAG). A final quality control by qPCR was performed by the sequencing provider before paired-end 150 nt sequencing on a NovaSeq6000 S4 (Illumina). More than 940 Gbp of reads were produced, with a minimum of 19 million paired-end reads per sample.

RNA-seq data preprocessing and alignment. Stranded paired-end reads were processed using Trimgalore (v0.6.7)⁵⁵ using default parameters. Trimmed reads were aligned to the human reference genome version hg38 using STAR⁵⁶ with default parameters. STAR indexes were built using the ENSEMBL annotation version GRCh38.101. SAM files were converted to BAM and sorted using samamba (v0.6.70)⁵⁷. Gene counts were obtained with the featureCounts function from the Rsubread package⁵⁸ with the gtf file corresponding to ENSEMBL version GRCh38.101 and parameters set to isPairedEnd = TRUE and strand-Specific = 2. Technical replicates were collapsed by adding the corresponding columns in the count matrix.

RNA-seq differential expression and functional enrichment. All analyses were performed in the R programming language version 4.1.3⁵⁹ unless otherwise stated. Differential analyses were performed using the DESeq2 package⁶⁰ with the experimental batch as a covariate.

Functional enrichment was performed using the roastgsa package⁶¹. Briefly, a rotation-based approach for enrichment⁶² implemented in the R package limma⁶³ is used to represent the null distribution. The maxmean enrichment statistic proposed in ref. 64, under restandardization, was considered for competitive testing. Gene set analysis was performed employing the regularized VST transformed matrix from DESeq2, in which low variance genes (genes with standard deviation lower than 0.135) were filtered out. The Broad Hallmarks gene set collection⁶⁵ was downloaded from refs. 65,66.

Gene Set Enrichment Analysis for MFNa and MFi treatments. GSEA Pre-ranked was used to perform a gene set enrichment analysis of annotations from the MsigDB Hallmarks with standard GSEA analysis settings. The input for enrichment consisted of the LFC values. We used the GO biological process dataset as the reference gene annotation database. We used the list ranked by statistic, setting 'gene set' as the permutation method, and ran it with 1000 permutations for Kolmogorov-Smirnov correction for multiple testing, including only gene sets with more than 15 members and less than 500 members. GSEA Enrichment data were obtained and ranked according to their FDR *q*-value. We considered significantly enriched those gene sets with FDR *q*-value <0.25.

Detection of mitochondrial Heavy (H) and Light (L) strands RNA in cytosolic extracts from cells and in mouse tissues

For RNA isolated from cytosolic fractions or extracted from brain samples, SuperScript IV reverse transcriptase (18090050, Invitrogen™) was used to synthesize the cDNA using primers in Supplementary Table 5. RT-qPCR was performed using strand-specific primers containing CMV promoter sequences to target different genes as previously described⁶⁷. Primers used are listed in Supplementary Table 5-6.

Mitochondrial DNA content

DNA was extracted from cell pellets using the DNeasy Blood and Tissue Kit (Qiagen). From the DNA extract, 10 ng per reaction were used to amplify DNA using specific primers for mitochondrial DNA (mtDNA) or nuclear DNA (nDNA) (Supplementary Table 7). Mitochondrial DNA content was calculated as follows:

- a. $\Delta CT = (nDNA\ CT - mtDNA\ CT)$
- b. Relative mtDNA content = $2 \times 2^{\Delta CT}$

Two primer sets were used for each sample and the average was calculated.

Human gene expression analysis

To analyze mRNA expression in human specimens, we used the voyAGER database⁵⁰. Data for mitochondrial RNAs present in a cell-free form in the serum of aged individuals was taken from available data from previously published studies⁵¹.

Senescence-associated β-galactosidase (SABG) activity

For senescence-associated β-galactosidase staining, cells and OCT-frozen tissue sections were fixed in SABG fixation solution (PBS with 0.1 M EGTA, 1 M MgCl2, and 50% glutaraldehyde) for 15 min at room temperature and washed 2 times with PBS. Then, a staining solution (PBS with 1 M MgCl2, 0.5 M K4[Fe(CN)6], and 0.5 M K3[Fe(CN)6]) at pH 6 with 1 mg/ml X-Gal diluted in DMF (all from Sigma) was added and incubated overnight at 37 °C in a CO2-free incubator. Samples were then washed in PBS and visualized using a Nikon Eclipse TS2 brightfield microscope.

Immunofluorescence and super-resolution microscopy image processing

Cells were fixed in 4% paraformaldehyde for 10 min, permeabilized with 0.1% triton, and blocked in 10% FBS + 0.1% triton for 30 min. For

MAVS staining, blocking and incubation were done in 5% milk. Primary antibodies were used as indicated in Supplementary Table 1 overnight at 4 °C. Cells and tissues were washed three times with PBS and incubated with secondary antibody (1:500) for 1 h. They were then washed with PBS before mounting with Vectashield mounting medium with DAPI (Vector Laboratories). Confocal images were obtained using the super-resolution Airyscan detector of the ZEISS Elyra 7 microscope at ×64 magnification and 1.8NA. Mitochondrial staining was achieved by incubating cells with MitoTracker Red CMXRos (Thermo Fisher) at 200 nM for 30 min prior to fixation. The secondary antibodies used were Alexa Fluor 488, Alexa Fluor 568, and Alexa Fluor 647. Image processing and quantifications were performed using ImageJ software. All quantifications were done on stacks of images.

Immunofluorescence of dsRNA with J2 antibody

Cells were grown in a Nunc Lab-Tek II Chamber Slide System 24–48 h before treatment. For transcription inhibitor treatment, cells were treated with dimethylsulfoxide (DMSO), actinomycin D (1 μM, 2 h) or IMT1 at the indicated times and concentrations. Cells were incubated with MitoTracker™ Red CMXRos (7512, Thermo Fisher) at 200 nM for 30 min at 37 °C before fixing in 3.7% PFA-DMEM for 15 min at 37 °C. Tissue cryosections (OCT) were fixed in 4% paraformaldehyde for 10 min. Cells and tissues were washed three times with PBS and permeabilized with 0.25% Triton X-100 in PBS, washed with 0.05% Tween20 in PBS, and incubated with 3% BSA in PBS for 30 min at room temperature. Primary antibody anti-dsRNA (J2) was used at 1:200 in 3% BSA in PBS for 1 h at room temperature. They were washed three times with 0.05% Tween20-PBS and incubated with secondary goat anti-mouse IgG (H+L) conjugated with Alexa Fluor 488 at (1:300) concentration. Then, washed three times with 0.05% Tween20-PBS, PBS, and mounted with a Vectashield mounting medium with DAPI (Vector Laboratories). Z-stack images were collected with a super-resolution Airyscan detector of ZEISS Elyra 7 microscope at ×64 magnification and 1.8NA. Images were analyzed using ImageJ.

Colocalization of dsRNA and MAVS with mitochondria

Cells were stained as described in the “Immunofluorescence of dsRNA with j2 antibody” or “Immunofluorescence and super-resolution microscopy image processing” sections for dsRNA and MAVS staining, respectively. Cells were incubated with MitoTracker™ Red CMXRos (7512, Thermo Fisher) at 200 nM for 30 min at 37 °C before fixing in 3.7% PFA-DMEM for 15 min at 37 °C. Z-stack confocal images of microscopic slides were obtained using the super-resolution AiryScan detector of the ZEISS Elyra 7 microscope at ×64 magnification and 1.8NA. Image processing and quantifications were performed using ImageJ software. Colocalization of j2 spots or MAVS staining with mitochondria was based on fluorescence intensity from Mitotracker.

Live-cell microscopy

Cells were loaded with 200 nM Mitotracker Green (Life Technologies) or JC-10 (AAT Bioquest) in DMEM for 30 min at 37 °C. Cells were then washed and image acquisition was performed using a Spinning Disk microscope (Andor Revolution xD, Andor) equipped with a stage-top incubator and CO₂ control system. A total of 10 μm in 21 z-stacks were acquired at 512 × 512 pixel of format resolution with a 1.4 NA/60× oil immersion objective. Fiji-/ImageJ software was used to obtain a z projection of the z-stacks and quantified accordingly.

Mitochondrial morphology analysis

Cells were classified according to the following categories: (1) fragmented, if the vast majority of their mitochondria look like “dots”; (2) intermediate, if they have a mixture of both fragmented and elongated mitochondria but with no apparent branches; (3) elongated, if mitochondria are clearly long and have some branches; (4) hyperfused, if

mitochondria form highly tubular networks very interconnected or if they form clusters.

Membrane potential measurements

Cells were loaded with 10 μM JC-10 (Deltaclone) in a pre-warmed cell culture medium for 30 min at 37 °C. Cells were washed in a fresh medium and images acquired according to “Live-cell microscopy” section. As a positive control, membrane potential was dissipated in cells by 10 μM FCCP treatment.

Histological analysis

For formalin-fixed paraffin-embedded (FFPE) samples, tissues were fixed overnight at 4 °C with neutral buffered formalin (Sigma-Aldrich, #HT501128). Paraffin-embedded tissue sections (2–3 μm) were air-dried and dried overnight at 60 °C.

Sirius red staining

Picosirius Red Fast Green staining, tissue samples were incubated with the mordant Thiosemicarbazide 99% (TSC) (Sigma, T33405) for 10 min, washed in distilled water, incubated with 0.1% Fast green (Sigma, FCF F7552) for 20 min and rinsed with 1% acetic acid (Sigma, 320099) for 1 min. In all cases, samples were dehydrated and mounted with Mounting Medium, Toluene-Free (CS705, Dako, Agilent) using a Dako CoverStainer.

Iron detection by enhanced Perl’s Prussian blue (EPPB) staining

An Iron Stain Kit was used to identify iron pigments (AR15811-2, Artisan, Dako, Agilent), with some modifications. To enhance iron detection, we adapted the EPPB staining protocol by adding a blocking step with 5% normal goat serum (16210064, Life Technology) with 2.5% BSA (10735078001, Sigma) for 60 min followed with 30 min of peroxidase-blocking solution (S2023, Dako-Agilent) and a 30 min incubation with Liquid DAB+ Substrate Chromogen System (K3468, Dako-Agilent) on sections that had been previously stained with the Iron Stain kit.

Immunohistochemistry

Immunohistochemistry was performed manually, in a Ventana Discovery XT platform and in a Leica Bond RX platform. Primary antibodies were incubated on sections in a dilution and for the time as follows: p21 clone HUGO 291H/B5 (CNIO) RTU 60 min. Antigen retrieval for p21 was performed with Cell Conditioning 1 (CC1) buffer (Roche, 950-124). Secondary antibodies used were the OmniMap anti-Rat HRP (Roche, 760-4457) or OmniMapTM anti-Rb HRP (Roche, 760-4311). Blocking was done with Casein (Roche, 760-219). Antigen–antibody complexes were revealed with ChromoMap DAB Kit (Roche, 760-159). Washings were performed using the Wash Solution AR (AR10211-2, Dako, Agilent). Quenching of endogenous peroxidase was performed by 10 min of incubation with Peroxidase-Blocking Solution at RT (S2023, Dako, Agilent). Nonspecific unions were blocked using 5% of goat normal serum (16210064, Life technology) mixed with 2.5% BSA diluted in a wash buffer for 60 min at RT. Blocking of nonspecific endogenous mouse Ig staining was also performed using Mouse on mouse (M.O.M) Immunodetection Kit – (BMK-2202, Vector Laboratories). Secondary antibodies used were the BrightVision Poly-HRP-Anti Rabbit IgG Biotin-free, ready to use (DPVR-110 HRP, Immunologic), the HRP-Anti-Rat IgG (MP-7444, Vector) for 45 min or the Goat Anti-Mouse Immunoglobulins/HRP (Dako-Agilent, P0447) at 1:100 for 30 min. Antigen–antibody complexes were revealed with 3,3'-diaminobenzidine (K346811, Dako) or the DAB (Polymer) (Leica, RE7230-CE) with the same time exposure. Sections were counterstained with hematoxylin (CS700, Dako, Agilent) and mounted with Mounting Medium, Toluene-Free (CS705, Dako, Agilent) using a Dako CoverStainer. Specificity of staining was confirmed staining with the following isotype controls: rabbit IgG, polyclonal (Abcam, ab27478), the mouse IgG1, Kappa (NCG01)

(Abcam, ab81032), mouse IgG2a kappa (eBM2a) (eBioscienceTM, 14-4724-82) and the rat IgG (R&D Systems, 6-001-F).

Image acquisition and quantification of histological sections

Brightfield images were acquired with a NanoZoomer-2.0 HT C9600 digital scanner (Hamamatsu) equipped with a 20 \times objective. All images were visualized with a gamma correction set at 1.8 in the image control panel of the NDP.view 2 U12388-01 software (Hamamatsu, Photonics, France). Image quantification was performed in the QuPath software.

Electron microscopy analysis

Cells were fixed at 4 °C with a mixture of 2% PFA and 2.5% glutaraldehyde in 0.1M phosphate buffer (PB), then scrapped, pelleted, washed in PB, then postfixed with 1% osmium tetroxide and 0.8% potassium ferrocyanide. After that, samples were dehydrated with acetone and finally embedded in Spurr resin. Ultrathin sections (60 nm) were obtained using an Ultracut E (Reichert) and picked up on copper grids and observed with the JEM 1011 (JEOL, Japan) electron microscope, operating at 80 kV. Micrographs were taken with a camera (Orius 1200A; Gatan, USA) using the DigitalMicrograph software package (Gatan, USA). Electron micrographs were processed using Adobe Photoshop CS6 (13.0.1) (Adobe Systems). All mitochondria in randomly selected cells showing nuclear section per EM field (each field is the square hole of a 200mesh grid) were examined at a magnification of 60.000 \times and 120.000 \times . The proportion of cells containing MDV-related structures and the mean number of mitochondria per cell showing these structures was estimated in a total of 30 control and 30 bleomycin-treated cells from five EM fields.

Statistics analysis

For mouse experiments, no specific blinding method was used but mice in each simple group were selected randomly. The sample size (n) of each experimental group is described in each corresponding figure legend. Unless otherwise specified, results from each group were averaged and expressed as means + standard error of the mean (represented as error bars). T-test was used for comparison between 2 groups and one-way ANOVA analysis was used for comparisons among 3 or more groups. Two-way ANOVA analysis was used to examine the influence of two different independent variables. The Statistics program Prism (GraphPad Prism 9) was used for analysis. Statistical significance was set at a *P*-value < 0.05

Reporting summary

Further information on research design is available in the Nature Portfolio Reporting Summary linked to this article.

Data availability

The RNA-sequencing data generated in this study have been deposited in the GEO database under accession code [GSE236521](#). Previously published datasets that were used for analysis in the current study are [GSE112289](#), RNA-seq of cell-free RNA in the serum of young and old humans; voyAGER database⁵⁰, mRNA expression in human specimens. All of the data needed to reproduce the results presented here can be found in the manuscript, figures, and supplementary materials. Source data are provided with this paper.

References

1. Abid, S. et al. *Cellular Senescence in Disease* (eds Muñoz-Espín, D. & Serrano, M.) xv-xix (Academic Press, 2022).
2. Kale, A. et al. Role of immune cells in the removal of deleterious senescent cells. *Immun. Ageing* **17**, 1–9 (2020).
3. Chaib, S., Tchkonia, T. & Kirkland, J. L. Cellular senescence and senolytics: the path to the clinic. *Nat. Med.* **28**, 1556–1568 (2022).
4. Birch, J. & Gil, J. Senescence and the SASP: Many therapeutic avenues. *Genes Dev.* **34**, 1565–1576 (2020).
5. Martini, H. & Passos, J. F. Cellular senescence: all roads lead to mitochondria. *FEBS J.* **290**, 1186–1202 (2023).
6. Wiley, C. D. et al. Mitochondrial dysfunction induces senescence with a distinct secretory phenotype. *Cell Metab.* **23**, 303–314 (2016).
7. Correia-Melo, C. et al. Mitochondria are required for pro-ageing features of the senescent phenotype. *EMBO J.* **35**, 724–742 (2016).
8. Vizioli, M. G. et al. Mitochondria-to-nucleus retrograde signaling drives formation of cytoplasmic chromatin and inflammation in senescence. *Genes Dev.* **34**, 428–445 (2020).
9. Victorelli, S. et al. Apoptotic stress causes mtDNA release during senescence and drives the SASP. *Nature* **622**, 627–636 (2023).
10. Iske, J. et al. Senolytics prevent mt-DNA-induced inflammation and promote the survival of aged organs following transplantation. *Nat. Commun.* **11**, 4289 (2020).
11. Marchi, S., Guilbaud, E., Tait, S. W. G., Yamazaki, T. & Galluzzi, L. Mitochondrial control of inflammation. *Nat. Rev. Immunol.* **23**, 159–173 (2023).
12. Newman, L. E. & Shadel, G. S. Mitochondrial DNA release in innate immune signaling. *Annu. Rev. Biochem.* **92**, 299–332 (2023).
13. Xian, H. & Karin, M. Oxidized mitochondrial DNA: a protective signal gone awry. *Trends Immunol.* **44**, 188–200 (2023).
14. Xavier, V. J. & Martinou, J. C. RNA granules in the mitochondria and their organization under mitochondrial stresses. *Int. J. Mol. Sci.* **22**, 9502 (2021).
15. Dhir, A. et al. Mitochondrial double-stranded RNA triggers antiviral signalling in humans. *Nature* **560**, 238–242 (2018).
16. Kim, S. et al. Mitochondrial double-stranded RNAs govern the stress response in chondrocytes to promote osteoarthritis development. *Cell Rep.* **40**, 111178 (2022).
17. Zhu, Y. et al. Polynucleotide phosphorylase protects against renal tubular injury via blocking mt-dsRNA-PKR-eIF2 α axis. *Nat. Commun.* **14**, 1223 (2023).
18. Lee, H. et al. Cell type-specific transcriptomics reveals that mutant huntingtin leads to mitochondrial RNA release and neuronal innate immune activation. *Neuron* **107**, 891–908.e8 (2020).
19. Tigano, M., Vargas, D. C., Tremblay-Belzile, S., Fu, Y. & Sfeir, A. Nuclear sensing of breaks in mitochondrial DNA enhances immune surveillance. *Nature* **591**, 477–481 (2021).
20. Rice, G. I. et al. Mutations in ADAR1 cause Aicardi-Goutières syndrome associated with a type I interferon signature. *Nat. Genet.* **44**, 1243–1248 (2012).
21. Chen, Y. G. & Hur, S. Cellular origins of dsRNA, their recognition and consequences. *Nat. Rev. Mol. Cell Biol.* **23**, 286–301 (2022).
22. Schonborn, J. et al. Monoclonal antibodies to double-stranded RNA as probes of RNA structure in crude nucleic acid extracts. *Nucleic Acids Res.* **19**, 2993–3000 (1991).
23. Riley, J. S. et al. Mitochondrial inner membrane permeabilisation enables mt DNA release during apoptosis. *EMBO J.* **37**, e99238 (2018).
24. McArthur, K. et al. BAK/BAX macropores facilitate mitochondrial herniation and mtDNA efflux during apoptosis. *Science* **359**, eaao6047 (2018).
25. Matilainen, S. et al. Defective mitochondrial RNA processing due to PNPT1 variants causes Leigh syndrome. *Hum. Mol. Genet.* **26**, 3352–3361 (2017).
26. Bonekamp, N. A. et al. Small-molecule inhibitors of human mitochondrial DNA transcription. *Nature* **588**, 712–716 (2020).
27. Laberge, R. M. et al. MTOR regulates the pro-tumorigenic senescence-associated secretory phenotype by promoting IL1A translation. *Nat. Cell Biol.* **17**, 1049–1061 (2015).

28. Herranz, N. et al. mTOR regulates MAPKAPK2 translation to control the senescence-associated secretory phenotype. *Nat. Cell Biol.* **17**, 1205–1217 (2015).
29. De Cecco, M. et al. L1 drives IFN in senescent cells and promotes age-associated inflammation. *Nature* **566**, 73–78 (2019).
30. Liu, X. et al. Resurrection of endogenous retroviruses during aging reinforces senescence. *Cell* **186**, 287–304.e26 (2023).
31. Song, B., Shiromoto, Y., Minakuchi, M. & Nishikura, K. The role of RNA editing enzyme ADAR1 in human disease. *Wiley Interdiscip. Rev. RNA* **13**, e1665 (2022).
32. Glück, S. et al. Innate immune sensing of cytosolic chromatin fragments through cGAS promotes senescence. *Nat. Cell Biol.* **19**, 1061–1070 (2017).
33. Dou, Z. et al. Cytoplasmic chromatin triggers inflammation in senescence and cancer. *Nature* **550**, 402–406 (2017).
34. Takahashi, A. et al. Downregulation of cytoplasmic DNases is implicated in cytoplasmic DNA accumulation and SASP in senescent cells. *Nat. Commun.* **9**, 1–12 (2018).
35. Ye, J. & Maniatis, T. A prion-like trigger of antiviral signaling. *Cell* **146**, 348–350 (2011).
36. Castanier, C., Garcin, D., Vazquez, A. & Arnoult, D. Mitochondrial dynamics regulate the RIG-I-like receptor antiviral pathway. *EMBO Rep.* **11**, 133–138 (2010).
37. Kim, S. J. et al. Hepatitis C virus triggers mitochondrial fission and attenuates apoptosis to promote viral persistence. *Proc. Natl Acad. Sci. USA* **111**, 6413–6418 (2014).
38. Martínez, J. et al. Mitofusins modulate the increase in mitochondrial length, bioenergetics and secretory phenotype in therapy-induced senescent melanoma cells. *Biochem. J.* **476**, 2463–2486 (2019).
39. Mai, S., Klinkenberg, M., Auburger, G., Bereiter-Hahn, J. & Jendrach, M. Decreased expression of Drp1 and Fis1 mediates mitochondrial elongation in senescent cells and enhances resistance to oxidative stress through PINK1. *J. Cell Sci.* **123**, 917–926 (2010).
40. Marin, I. et al. Cellular senescence is immunogenic and promotes antitumor immunity. *Cancer Discov.* **13**, 410–431 (2023).
41. Chen, H. A. et al. Senescence rewires microenvironment sensing to facilitate antitumor immunity. *Cancer Discov.* **13**, 433–453 (2023).
42. Onoguchi, K. et al. Virus-infection or 5'ppp-RNA activates antiviral signal through redistribution of IPS-1 mediated by MFN1. *PLoS Pathog.* **6**, e1001012 (2010).
43. Yasukawa, K. et al. Mitofusin 2 inhibits mitochondrial antiviral signaling. *Sci. Signal.* **2**, ra47 (2009).
44. Khodzhaeva, V. et al. Mitofusin 2 deficiency causes pro-inflammatory effects in human primary macrophages. *Front. Immunol.* **12**, 723683 (2021).
45. Zacharioudakis, E. et al. Modulating mitofusins to control mitochondrial function and signaling. *Nat. Commun.* **13**, 3775 (2022).
46. Muñoz-Espín, D. et al. A versatile drug delivery system targeting senescent cells. *EMBO Mol. Med.* **10**, 1–18 (2018).
47. Schafer, M. J., Haak, A. J., Tschumperlin, D. J. & LeBrasseur, N. K. Targeting senescent cells in fibrosis: pathology, paradox, and practical considerations. *Curr. Rheumatol. Rep.* **20**, 3 (2018).
48. Maus, M. et al. Iron accumulation drives fibrosis, senescence and the senescence-associated secretory phenotype. *Nat Metab* **5**, 2111–2130 (2023).
49. Borghesan, M., Hoogaars, W. M. H., Varela-Eirin, M., Talma, N. & Demaria, M. A senescence-centric view of aging: implications for longevity and disease. *Trends Cell Biol.* **30**, 777–791 (2020).
50. Schneider, A. L., Martins-Silva, R., Kaizeler, A., Saraiva-Agostinho, N. & Barbosa-Morais, N. L. voyAGEr, a free web interface for the analysis of age-related gene expression alterations in human tissues. *eLife* **12**, 1–19 (2024).
51. Dluzen, D. F. et al. Extracellular RNA profiles with human age. *Aging Cell* **17**, e12785 (2018).
52. Kim, Y. et al. PKR senses nuclear and mitochondrial signals by interacting with endogenous double-stranded RNAs. *Mol. Cell* **71**, 1051–1063.e6 (2018).
53. Sun, T. et al. A small subset of cytosolic dsRNAs must be edited by ADAR1 to evade MDA5-mediated autoimmunity. Preprint at *bioRxiv* <https://doi.org/10.1101/2022.08.29.505> (2022).
54. Killarney, S. T. et al. Executioner caspases restrict mitochondrial RNA-driven type I IFN induction during chemotherapy-induced apoptosis. *Nat. Commun.* **14**, 1399 (2023).
55. Krueger, F. TrimGalore: a wrapper around Cutadapt and FastQC to consistently apply adapter and quality trimming to FastQ files, with extra functionality for RRBS data. *GitHub* <https://github.com/FelixKrueger/TrimGalore> (2017).
56. Dobin, A. et al. STAR: ultrafast universal RNA-seq aligner. *Bioinformatics* **29**, 15–21 (2013).
57. Tarasov, A., Vilella, A. J., Cuppen, E., Nijman, I. J. & Prins, P. Sam-bamba: fast processing of NGS alignment formats. *Bioinformatics* **31**, 2032–2034 (2015).
58. Liao, Y., Smyth, G. K. & Shi, W. The R package Rsubread is easier, faster, cheaper and better for alignment and quantification of RNA sequencing reads. *Nucleic Acids Res.* **47**, e47 (2019).
59. Team, R. C. *R: A Language and Environment for Statistical Computing* (R Foundation for Statistical Computing. Vienna, Austria, 2020).
60. Love, M. I., Huber, W. & Anders, S. Moderated estimation of fold change and dispersion for RNA-seq data with DESeq2. *Genome Biol.* **15**, 550 (2014).
61. Caballe Mestres, A., Berenguer Llergo, A. & Stephan-Otto Attolini, C. A comparison of rotation-based scores for gene set analysis. *Bioinformatics* **24**, 408 (2023).
62. Wu, D. et al. ROAST: Rotation gene set tests for complex microarray experiments. *Bioinformatics* **26**, 2176–2182 (2010).
63. Ritchie, M. E. et al. Limma powers differential expression analyses for RNA-sequencing and microarray studies. *Nucleic Acids Res.* **43**, e47 (2015).
64. Efron, B. & Tibshirani, R. On testing the significance of sets of genes. *Ann. Appl. Stat.* **1**, 107–129 (2007).
65. Liberzon, A. et al. The molecular signatures database hallmark gene set collection. *Cell Syst.* **1**, 417–425 (2015).
66. Subramanian, A. et al. Gene set enrichment analysis: a knowledge-based approach for interpreting genome-wide expression profiles. *Proc. Natl Acad. Sci. USA* **102**, 15545–15550 (2005).
67. Kim, S., Yoon, J., Lee, K. & Kim, Y. Analysis of mitochondrial double-stranded RNAs in human cells. *STAR Protoc.* **4**, 102007 (2023).

Acknowledgements

We are grateful to the IRB Functional Genomics Unit and CRG/CNAG for library preparation and genomic sequencing, to the IRB microscopy unit, and to the CCIB flow cytometry facility for the technical support. We thank Ms. Tanya Liesel de Silva from the Gavathiotis lab for her technical assistance. V.L.P. was the recipient of a predoctoral contract from the Spanish Ministry of Education (FPU-18/05917). M.M. received funding from the European Union's Horizon 2020 research and innovation programme under the Marie Skłodowska-Curie grant agreement (No 794744), and from the Spanish Ministry of Science and Innovation (MCIN) (RYC2020-030652-I/AEI/10.13039/501100011033 and PID2022-142205OB-I00). E.Z., F.D.M.M. and E.G. were funded by the National Institutes of Health grants P01AG031782, P30AG038072, R01CA223243, and a Hevolution Foundation partnership grant. M.K. was funded by the Barcelona Institute of Science and Technology (BIST) and Asociación Española Contra el Cáncer (AECC; POSTD1802OSERR), and supported by the European Molecular Biology Organization (EMBO). Work in the laboratory of M.S. was funded by the IRB and “laCaixa” Foundation, and

by grants from the Spanish Ministry of Science co-funded by the European Regional Development Fund (ERDF) (SAF2017-82613-R), European Research Council (ERC-2014-AdG/669622), and Secretaria d'Universitats i Recerca del Departament d'Empresa i Coneixement of Catalonia (Grup de Recerca consolidat 2017 SGR 282).

Author contributions

V.L.P. conceptualized, designed, performed, and analyzed all experiments, contributed to bioinformatic data analysis, and co-wrote the manuscript. M.M. processed electron microscopy samples and helped with mouse experiments. E.Z., F.D.M.M. and E.G. contributed to experiments related to the activation or inhibition of MAVS and mitofusins, development and validation of the small molecule MFN1/2 activator and inhibitor. M.L. analyzed and interpreted electron microscopy samples. C.S.O.A. performed RNA-sequencing bioinformatics analysis. M.M., M.K., E.Z. and E.G. contributed to the general interpretation of the data. M.S. conceptualized, designed, and supervised the study, secured funding, analyzed the data, and co-wrote the manuscript. All authors discussed the results and commented on the manuscript.

Competing interests

M.S. is shareholder of Senolytic Therapeutics, Inc., Life Biosciences, Inc., Rejuveron Senescence Therapeutics, AG, and Altos Labs, Inc. M.S. has been consultant, until the end of 2022, of Rejuveron Senescence Therapeutics, AG, and Altos Labs, Inc. M.K. has ongoing or completed research contracts with Galapagos NV, Rejuveron Senescence Therapeutics, and mesoestetic®. E.Z. and E.G. are inventors in patents submitted by Albert Einstein College of Medicine that protect compounds, compositions, and methods for controlling mitofusins for the treatment of diseases and disorders. E.G. has received compensation for consulting and has equity ownership from BaxGen Therapeutics, Comorin Therapeutics, BeanPod Biosciences, Life Biosciences, and Stelexis Biosciences. The funders had no role in study design, data collection and analysis, decision to publish, or preparation of the manuscript. The remaining authors declare no competing interests.

Additional information

Supplementary information The online version contains supplementary material available at <https://doi.org/10.1038/s41467-024-51363-0>.

Correspondence and requests for materials should be addressed to Manuel Serrano.

Peer review information *Nature Communications* thanks Muhammet Gulen and the other, anonymous, reviewer(s) for their contribution to the peer review of this work. A peer review file is available.

Reprints and permissions information is available at <http://www.nature.com/reprints>

Publisher's note Springer Nature remains neutral with regard to jurisdictional claims in published maps and institutional affiliations.

Open Access This article is licensed under a Creative Commons Attribution-NonCommercial-NoDerivatives 4.0 International License, which permits any non-commercial use, sharing, distribution and reproduction in any medium or format, as long as you give appropriate credit to the original author(s) and the source, provide a link to the Creative Commons licence, and indicate if you modified the licensed material. You do not have permission under this licence to share adapted material derived from this article or parts of it. The images or other third party material in this article are included in the article's Creative Commons licence, unless indicated otherwise in a credit line to the material. If material is not included in the article's Creative Commons licence and your intended use is not permitted by statutory regulation or exceeds the permitted use, you will need to obtain permission directly from the copyright holder. To view a copy of this licence, visit <http://creativecommons.org/licenses/by-nc-nd/4.0/>.

© The Author(s) 2024